Supporting Information

Hierarchical Self-Assembly and Chiroptical Studies of Luminescent 4d-4f Cages

Zhuo Wang,[†,§,‡] Li-Peng Zhou,[†, ‡] Tong-Han Zhao,[‖] Li-Xuan Cai,[†] Xiao-Qing Guo,[†] Peng-Fei Duan,[*,‖] Qing-Fu Sun[*,†]

[†]State Key Laboratory of Structural Chemistry, Fujian Institute of Research on the Structure of Matter, Chinese Academy of Sciences, Fuzhou 350002, People's Republic of China.

[§]University of Chinese Academy of Sciences, Beijing 100049, People's Republic of China.

[‖]CAS Center for Excellence in Nanoscience, Division of Nanophotonic, CAS Key Laboratory of Nanosystem and Hierarchical Fabrication, National Center for Nanoscience and Technology (NCNST), No. 11 ZhongGuanCun BeiYiTiao, Beijing 100190, China.

Contents

1. Synthetic Procedures

The synthetic route of Ligand $1H^R$ and $1H^S$

Scheme S1 The synthetic route of the ligand **1H**

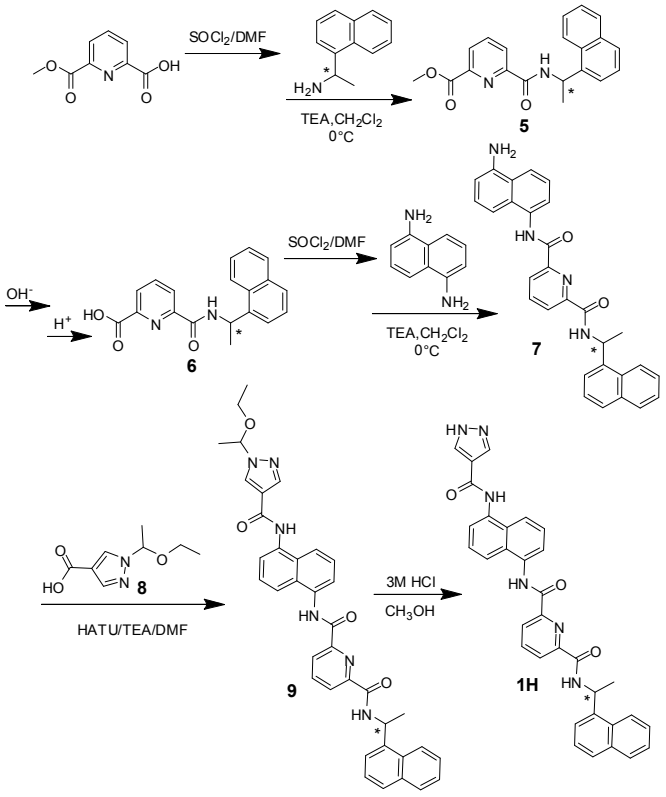

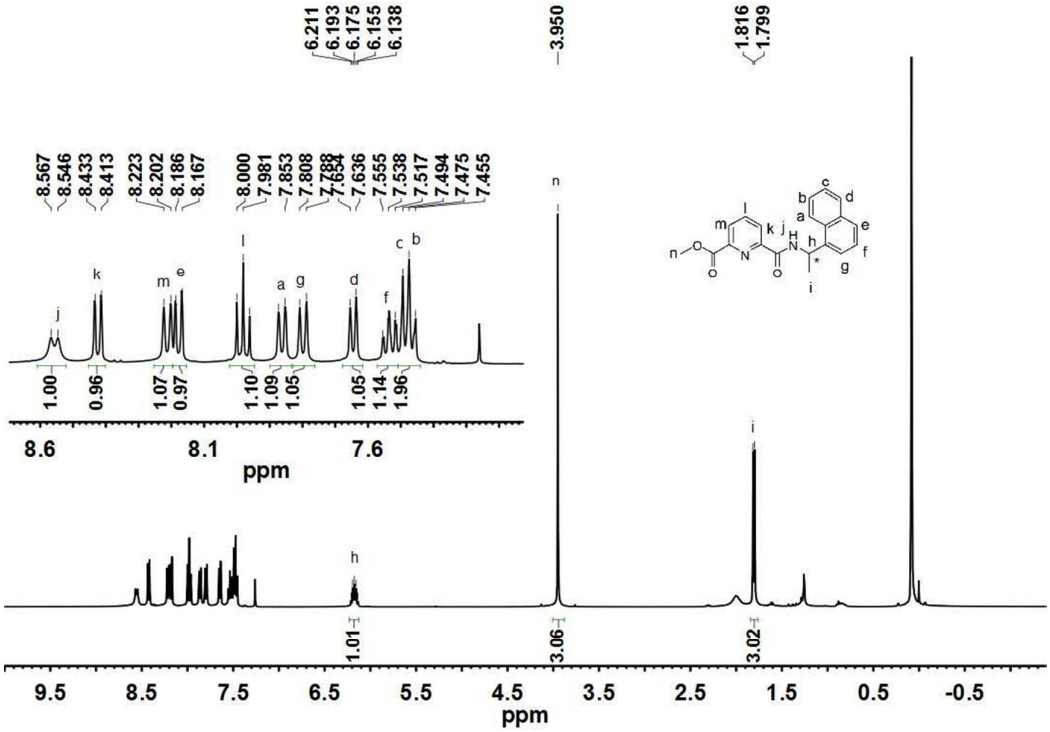

Figure S1. ^{1}H NMR spectra of **5**^{R} (400 MHz, $CDCl_3$, 298 K).

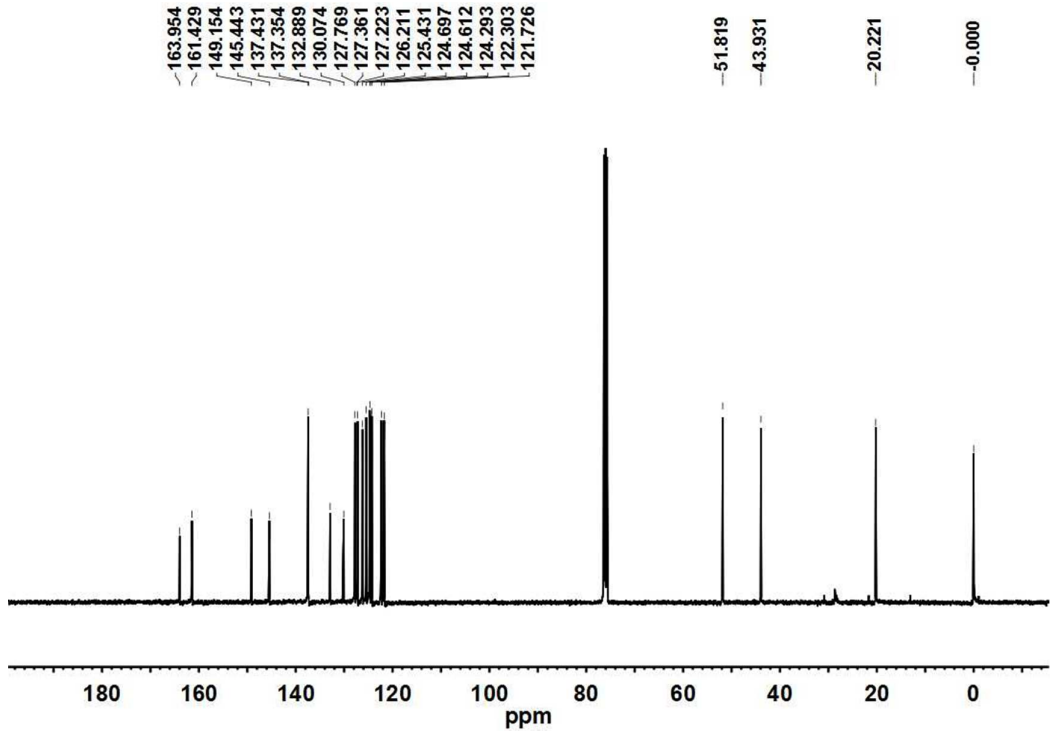

Figure S2. ^{13}C NMR spectrum of **5**^{R} (101 MHz, $CDCl_3$, 298 K).

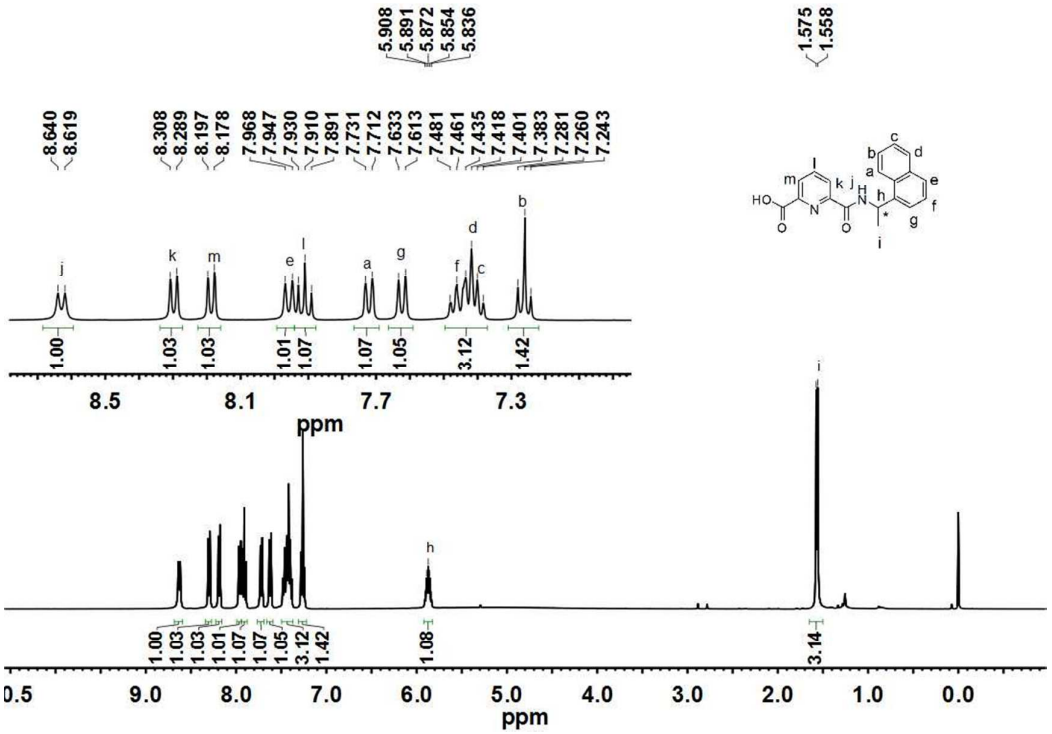

Figure S3. ^{1}H NMR spectra of **6**^{R} (400 MHz, $CDCl_3$, 298 K).

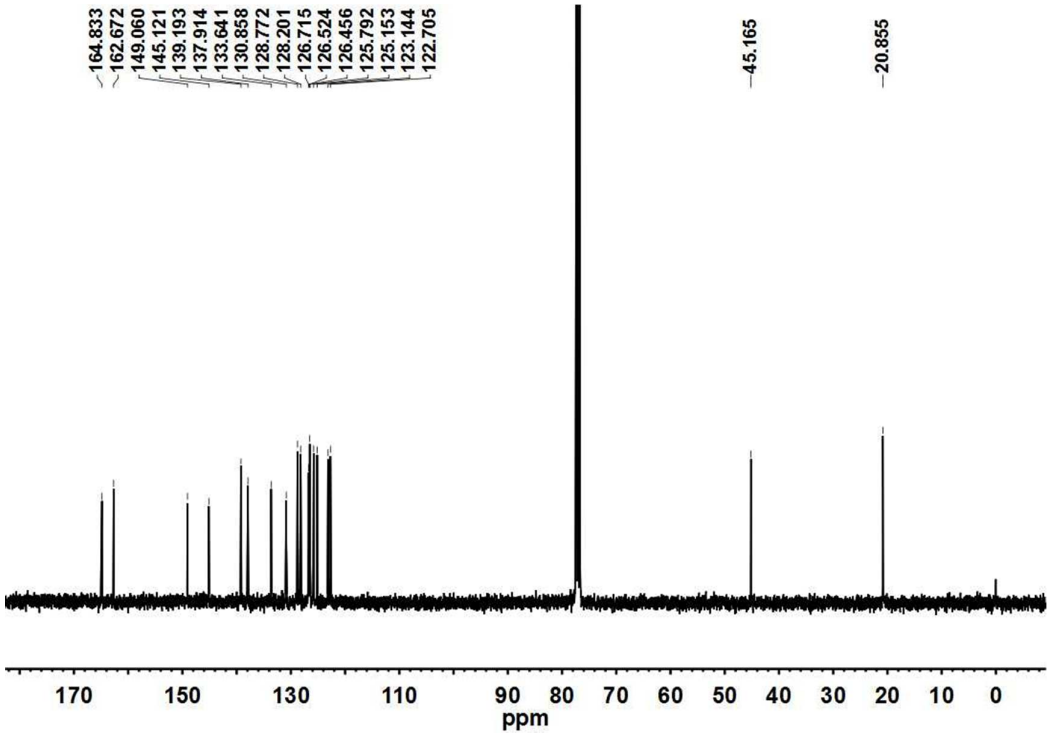

Figure S4. ^{13}C NMR spectrum of **6**^{R} (101 MHz, $CDCl_3$, 298 K).

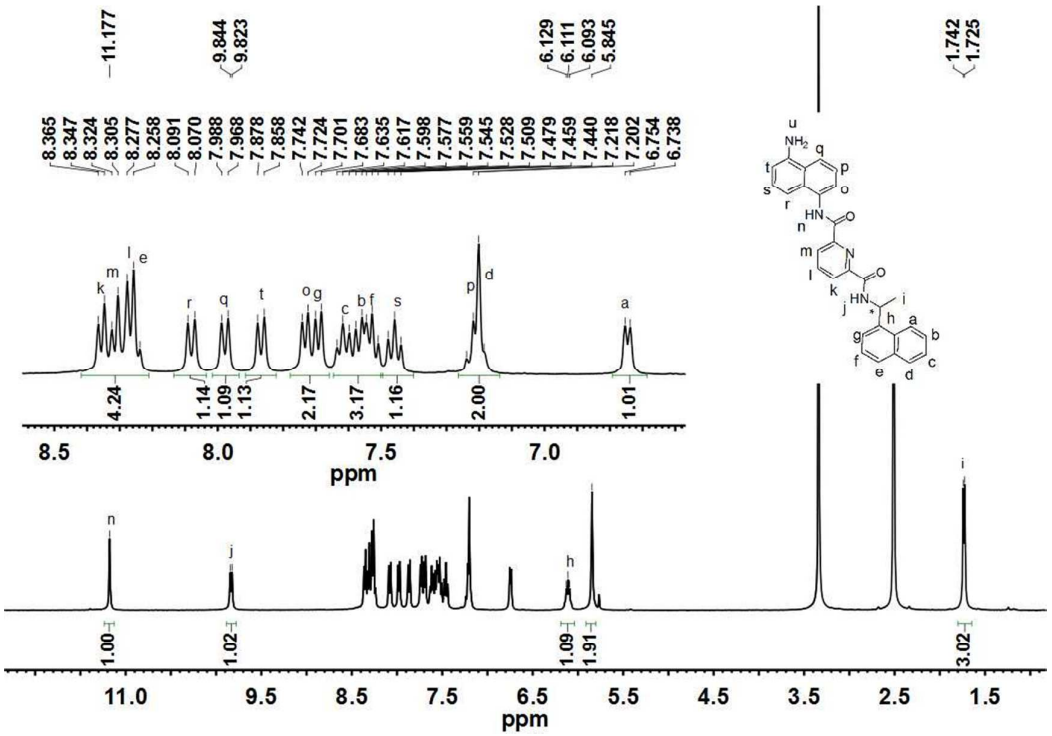

Figure S5. ^{1}H NMR spectra of **7**^{R} (400 MHz, d_6-DMSO, 298 K).

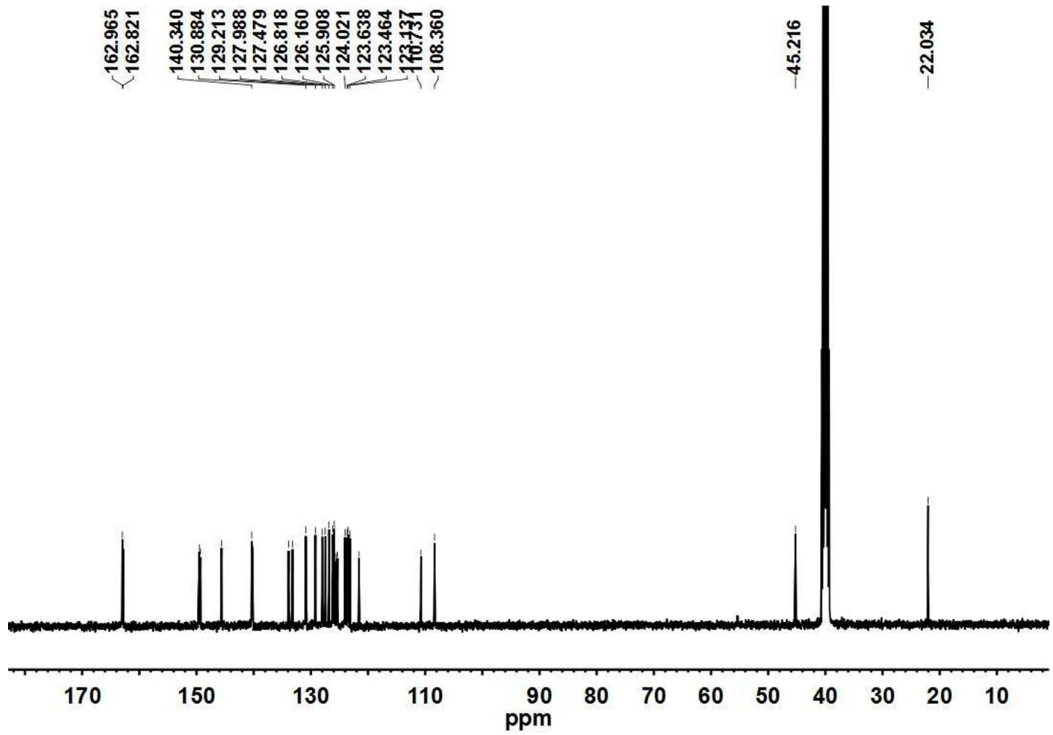

Figure S6. ^{13}C NMR spectrum of **7**^{R} (101 MHz, d_6-DMSO, 298 K).

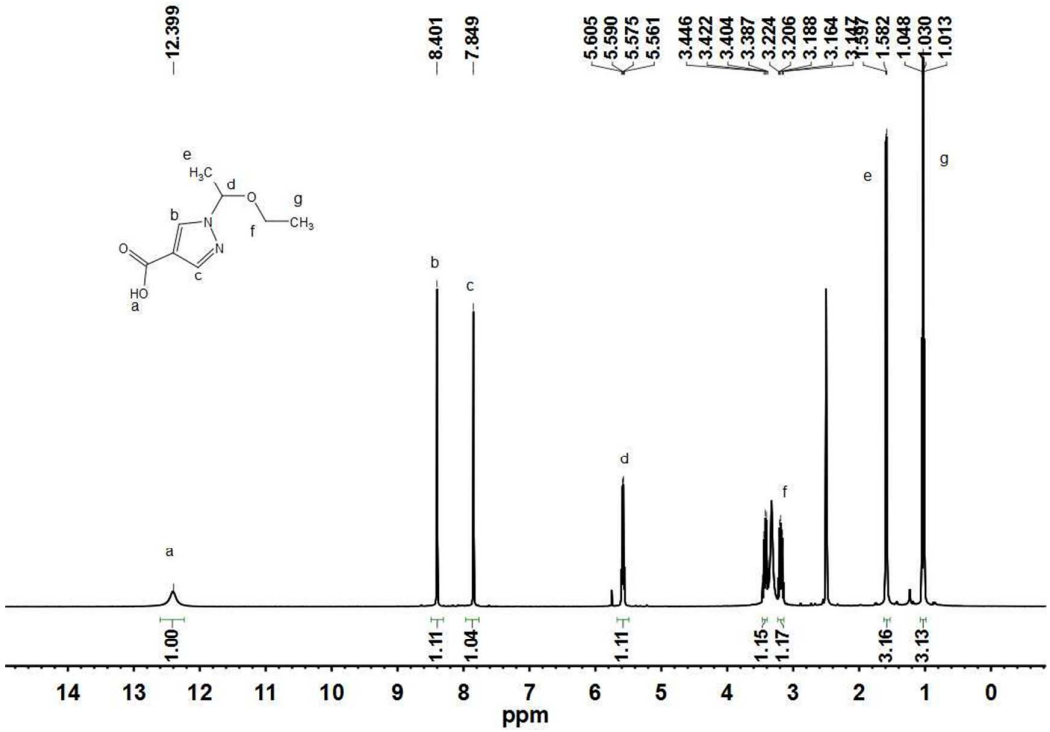

Figure S7. ^{1}H NMR spectrum of **8** (400 MHz, d_6-DMSO, 298 K).

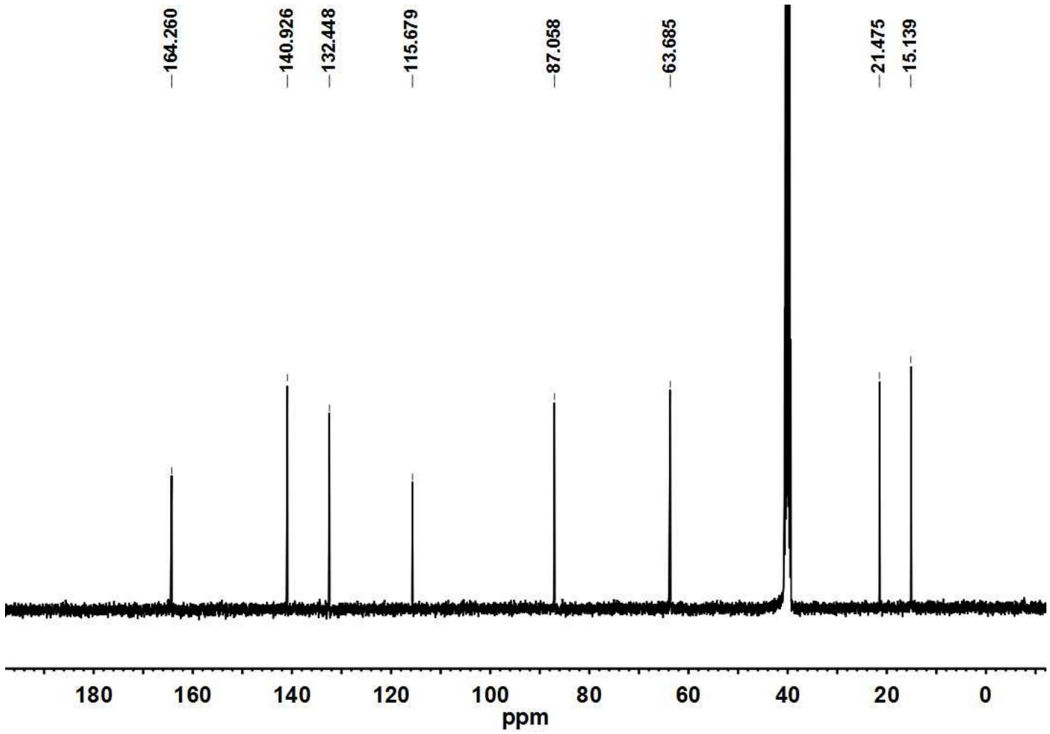

Figure S8. ^{13}C NMR spectrum of **8** (101 MHz, d_6-DMSO, 298 K).

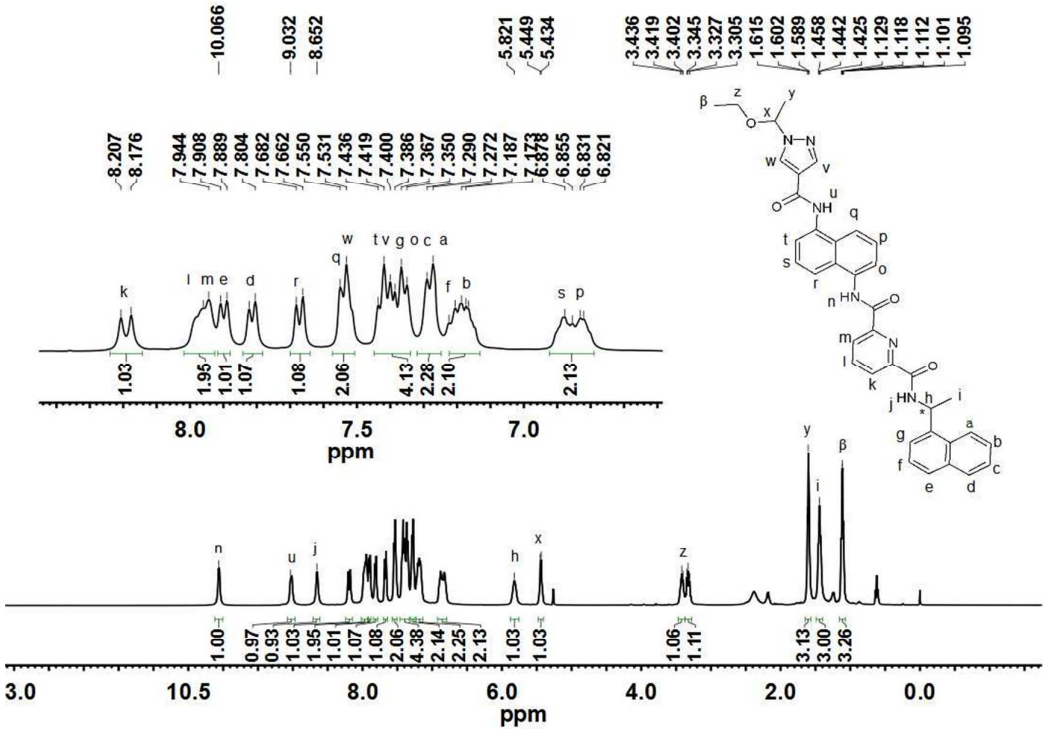

Figure S9. ^{1}H NMR spectra of **9**^{R} (400 MHz, $CDCl_3$, 298 K).

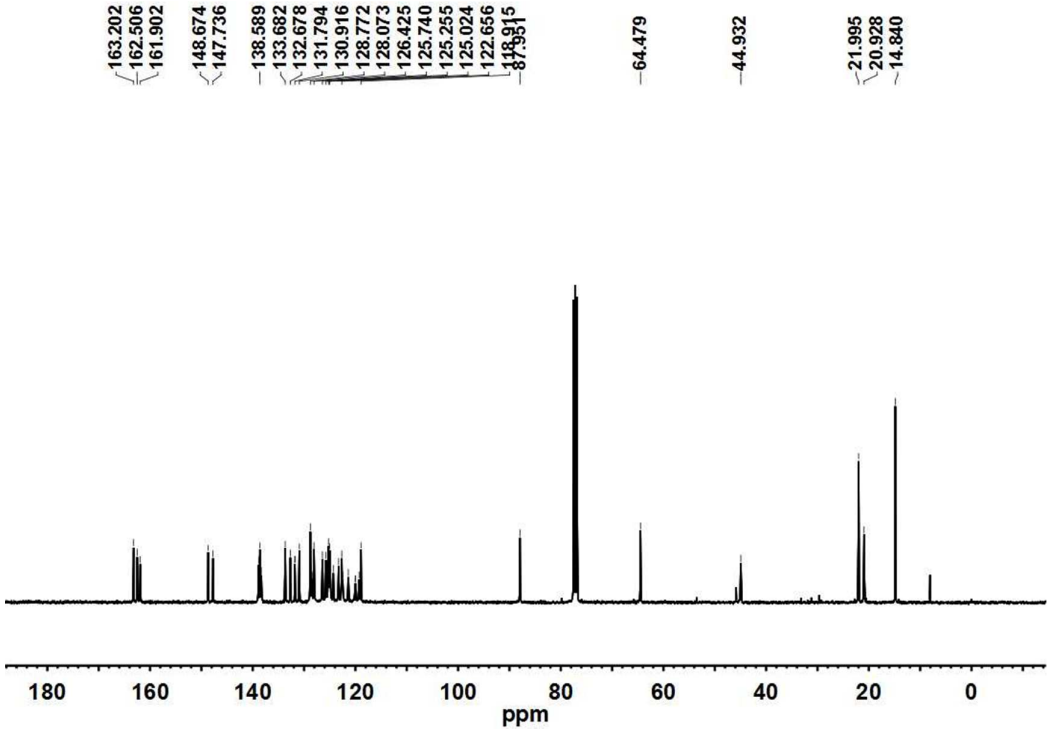

Figure S10. ^{13}C NMR spectrum of **9**^{R} (101 MHz, $CDCl_3$, 298 K).

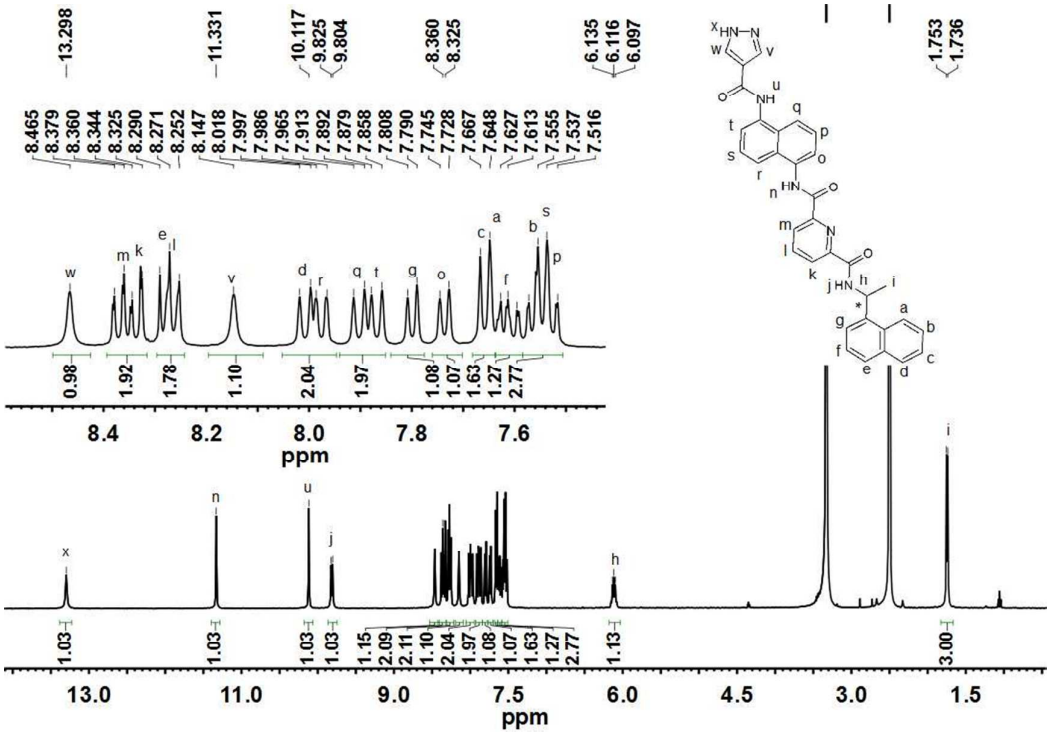

Figure S11. ^{1}H NMR spectra of **1H**^{R} (400 MHz, d_6-DMSO, 298 K).

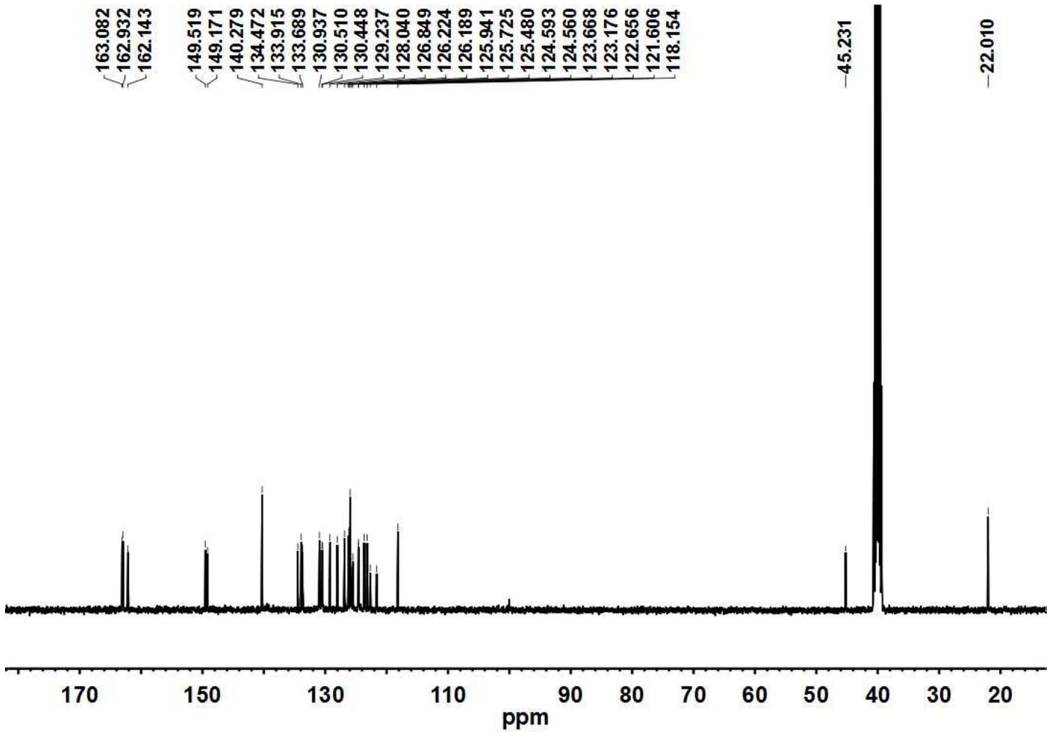

Figure S12. ^{13}C NMR spectrum of **1H**^{R} (101 MHz, d_6-DMSO, 298 K).

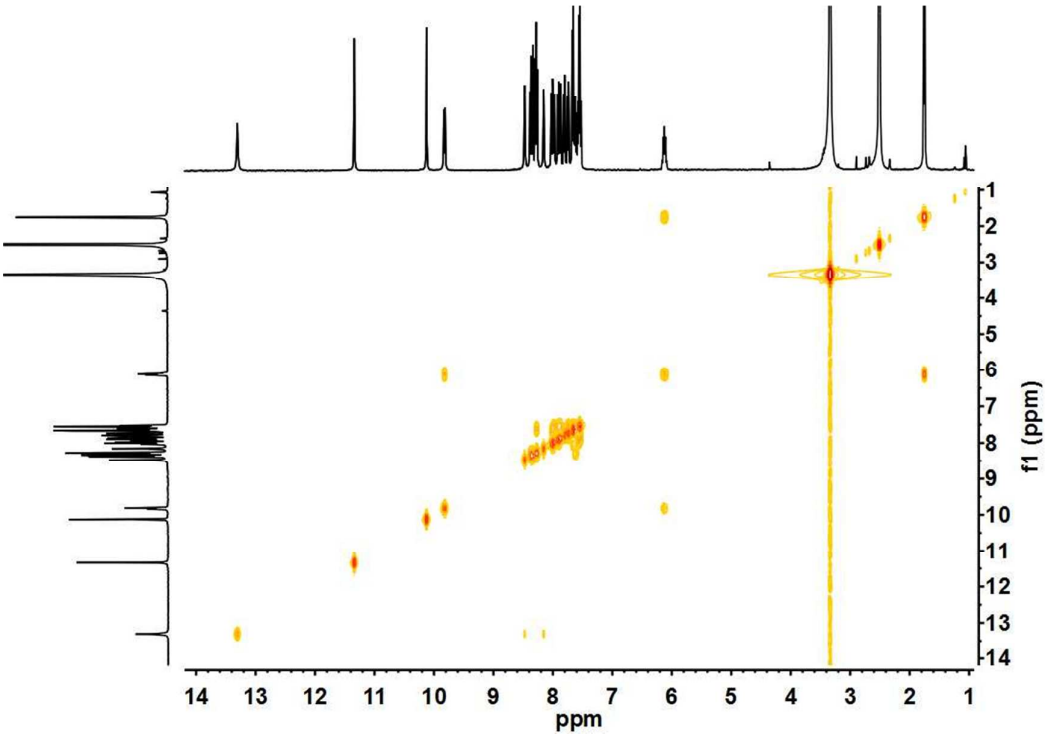

Figure S13. ^{1}H-^{1}H COSY NMR spectra of **1H**^{R} (400 MHz, d_6-DMSO, 298 K).

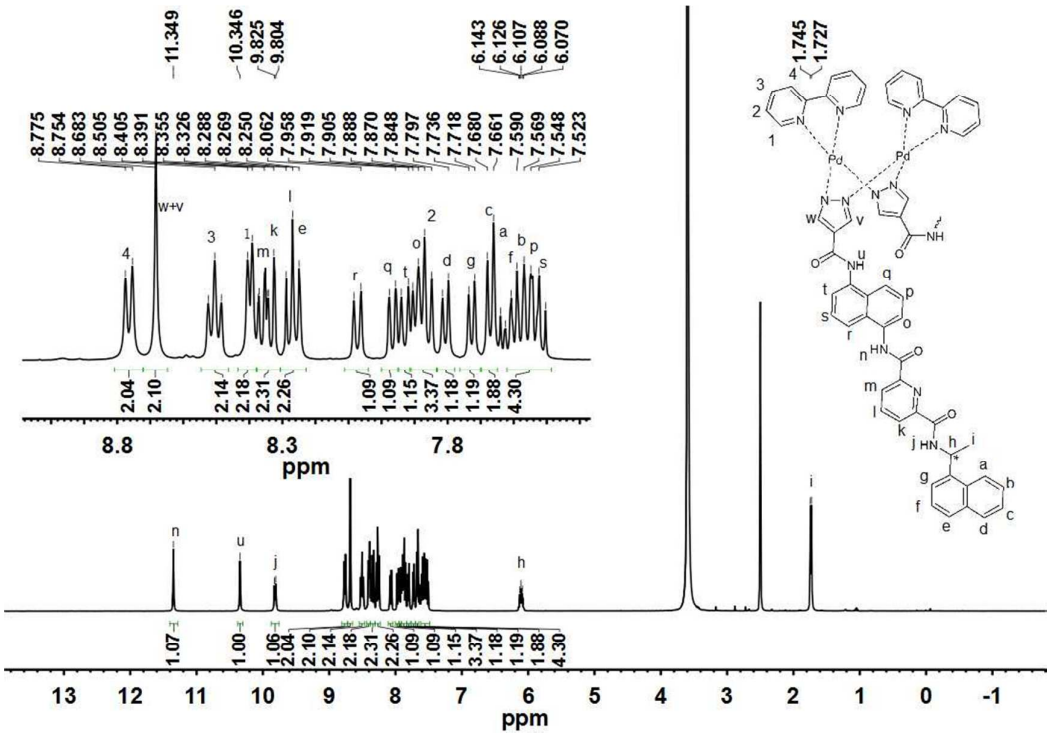

Figure S14**.** ^{1}H NMR spectrum of **2**^{R}•NO_3 (400 M Hz, d_6-DMSO, 298K).

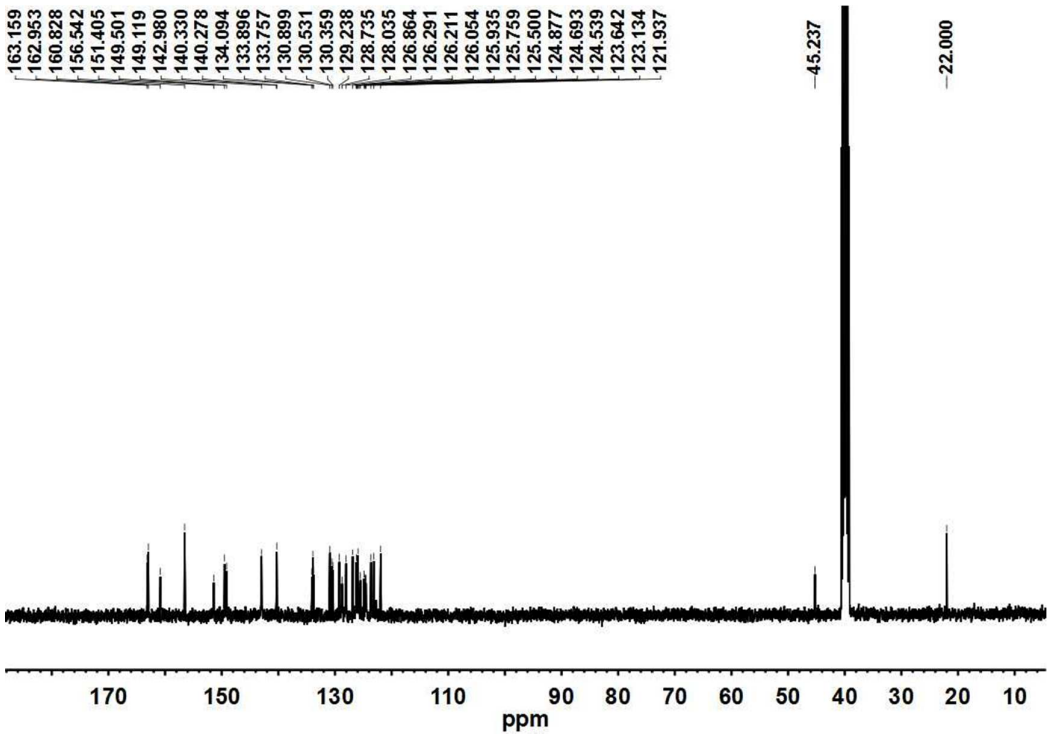

Figure S15. ^{13}C NMR spectrum of $\mathbf{2}^{R}$•NO_3 (101 MHz, d_6-DMSO, 298 K).

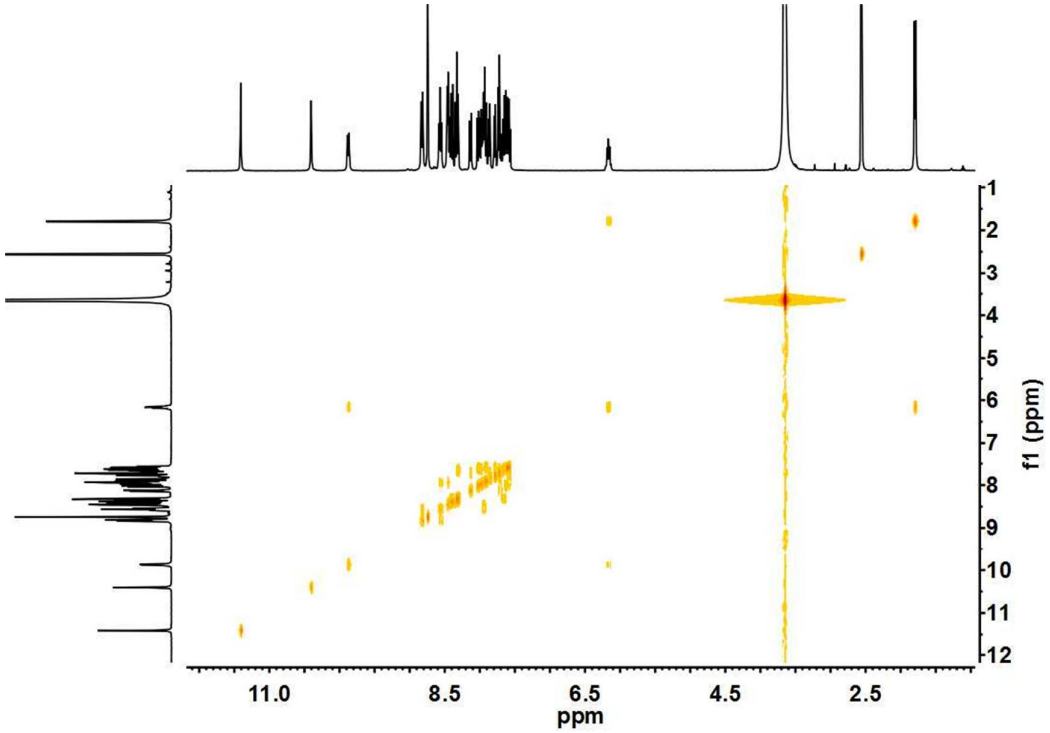

Figure S16. ^{1}H-^{1}H COSY NMR spectra of $\mathbf{2}^{R}$•NO_3 (400 MHz, d_6-DMSO, 298 K).

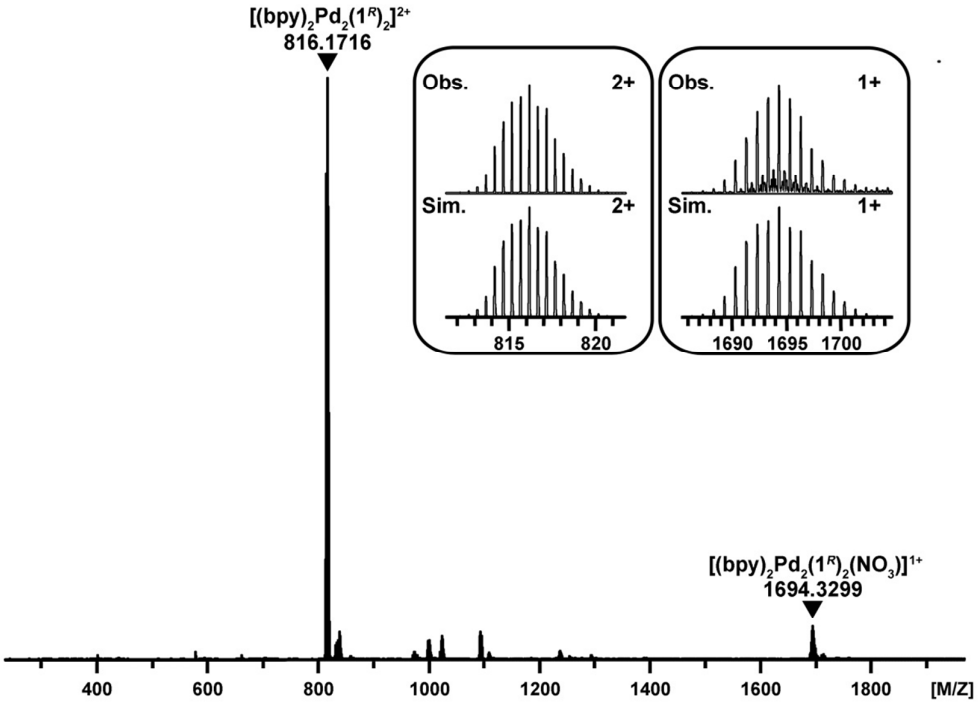

Figure S17. ESI-TOF-MS spectra of the self-assembly complex of $\mathbf{2}^{R}$•NO_3 with insets showing the observed and calculated isotopic patterns of the peaks at m/z 816.1716 and 1694.3299, corresponding to $[(bpy)_2Pd_2(\mathbf{1}^{R})_2]^{2+}$ and $[(bpy)_2Pd_2(\mathbf{1}^{R})_2(NO_3)]^{+}$, respectively.

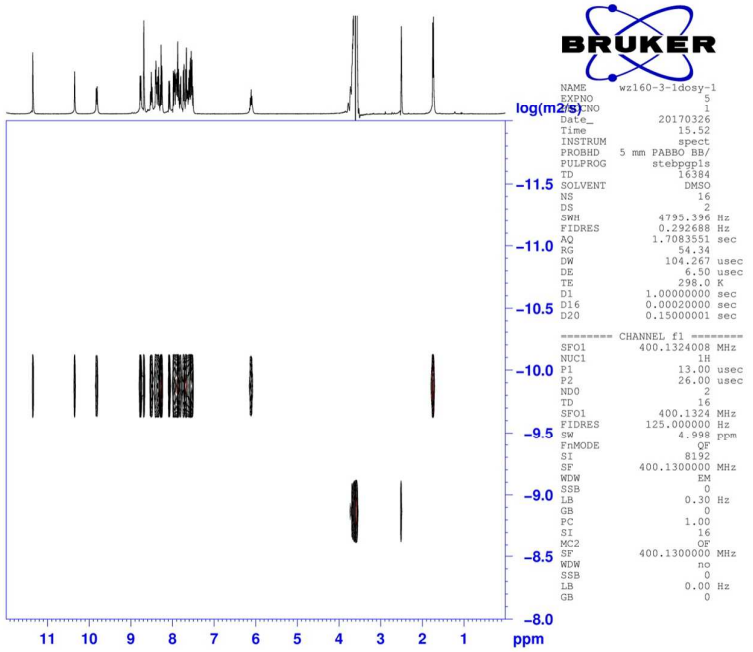

Figure S18. ^{1}H DOSY spectra of $\mathbf{2}^{R}$•NO_3 (log D = -9.871, r = 8.310Å, 400 MHz, d_6-DMSO, 298 K).

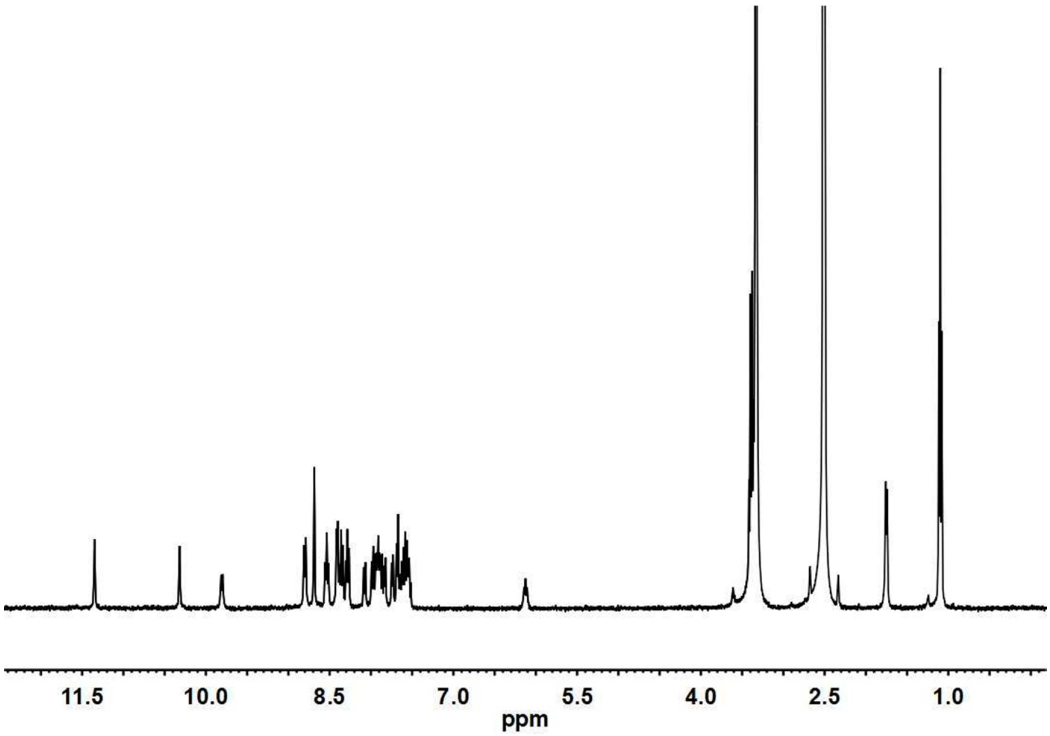

Figure S19. ^{1}H NMR spectrum of $\mathbf{2}^{R}$•OTf (400 MHz, d_6-DMSO, 298 K).

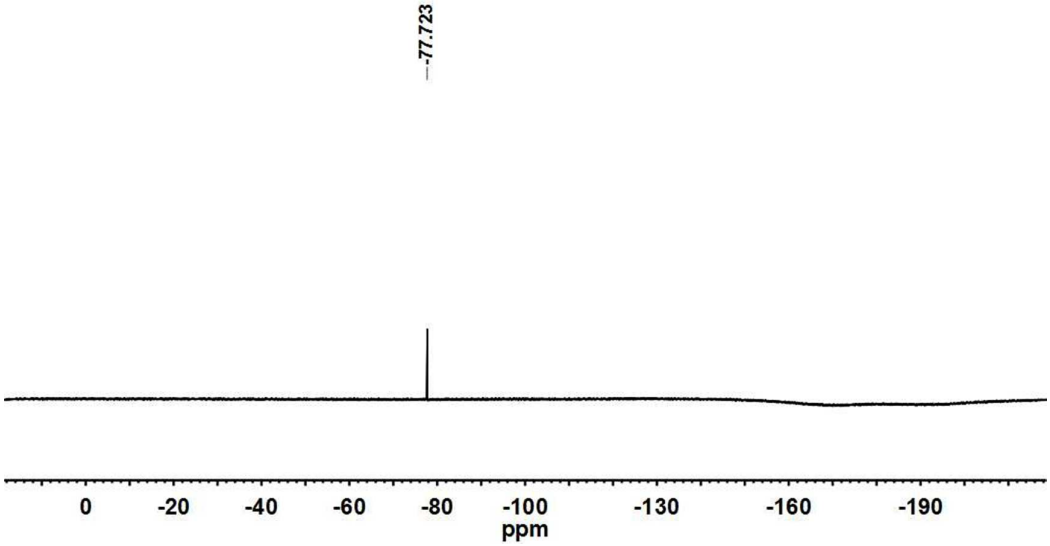

Figure S20. ^{19}F NMR spectrum of $\mathbf{2}^{R}$•OTf (400 MHz, d_6-DMSO, 298 K).

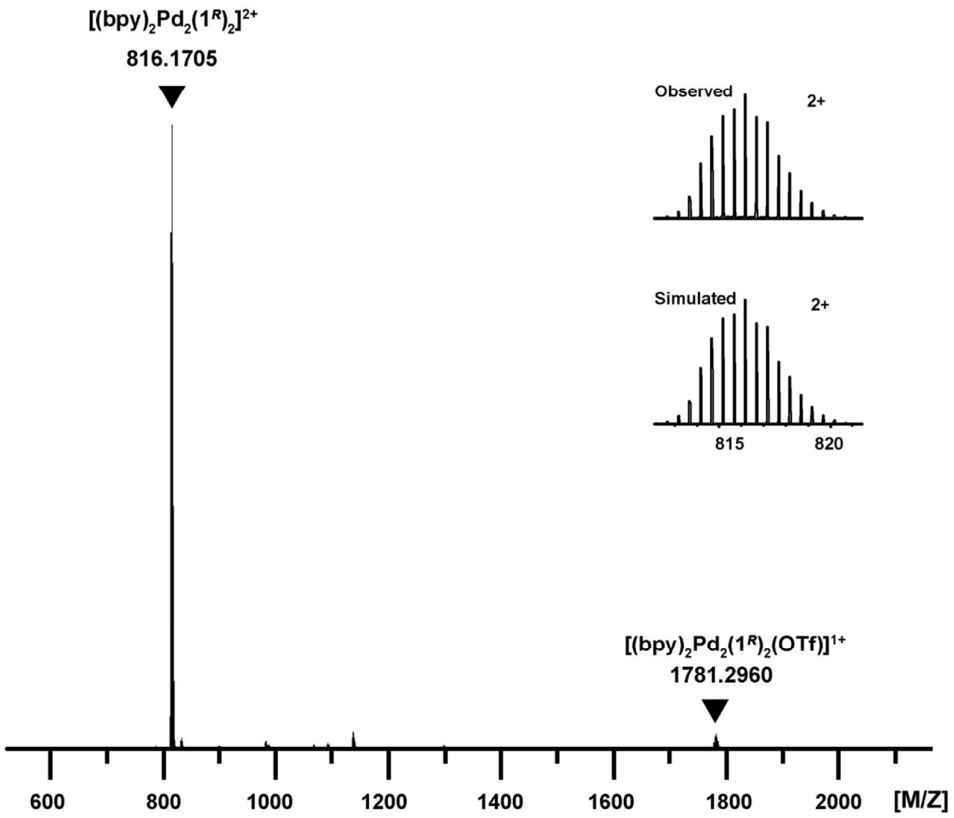

Figure S21. ESI-TOF-MS spectra of the self-assembly complex of $\mathbf{2}^{R}$•OTf with insets showing the observed and calculated isotopic patterns of the peaks at m/z 816.1705 corresponding to $[(bpy)_2Pd_2(\mathbf{1}^{R})_2]^{2+}$.

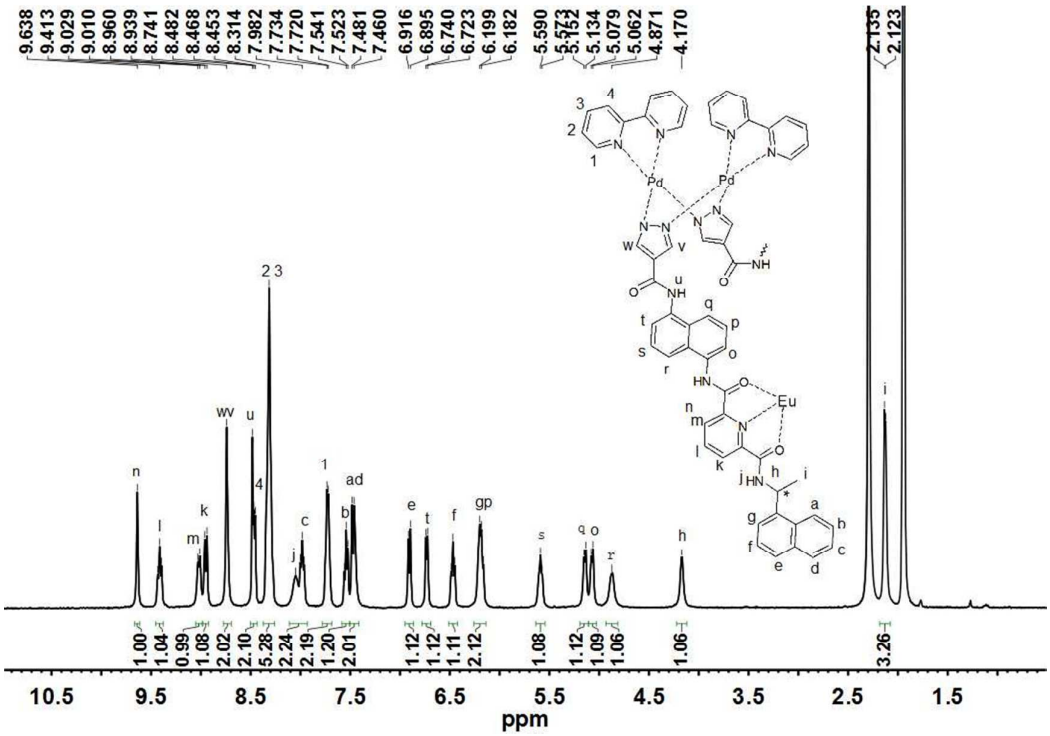

Figure S22. ^{1}H NMR spectra of **3**^{R}-Eu (400 MHz, CD_3CN, 298 K).

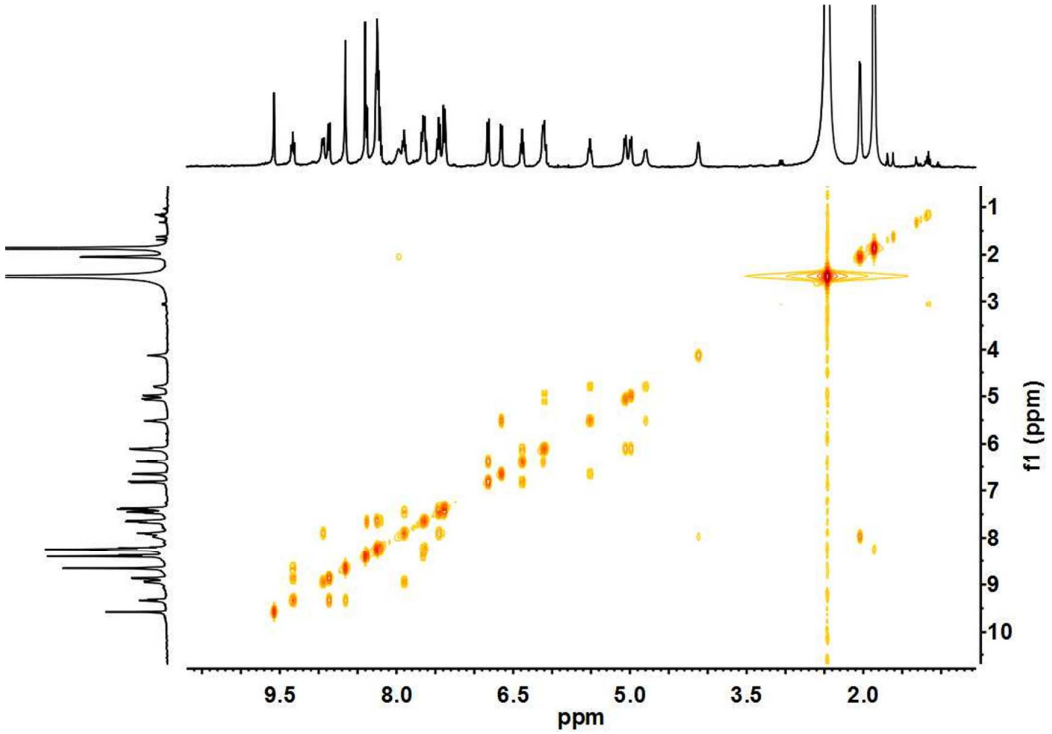

Figure S23. ^{1}H-^{1}H COSY NMR spectra of **3**^{R}-Eu (400 MHz, CD_3CN, 298 K).

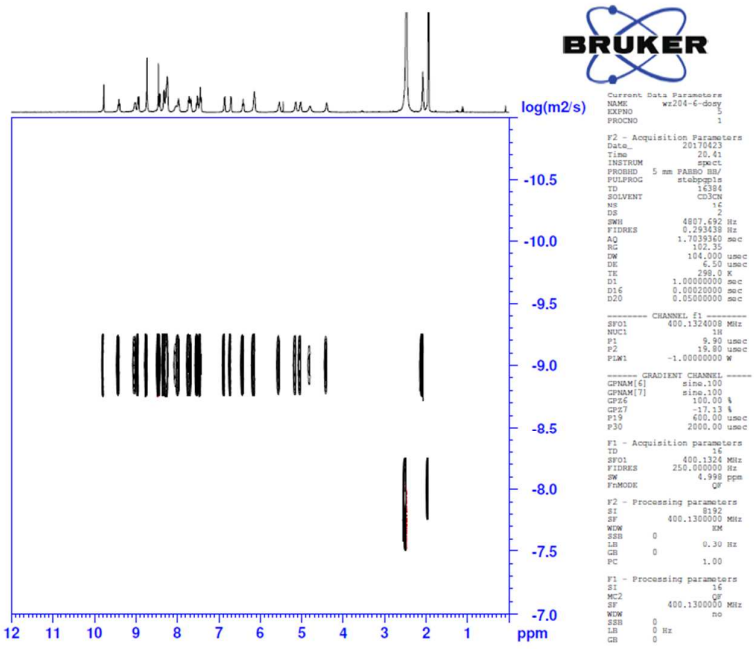

Figure S24. ^{1}H DOSY spectra of **3**^{R}-Eu (log D = -9.123, r = 8.443 Å, 400 MHz, CD_3CN, 298 K).

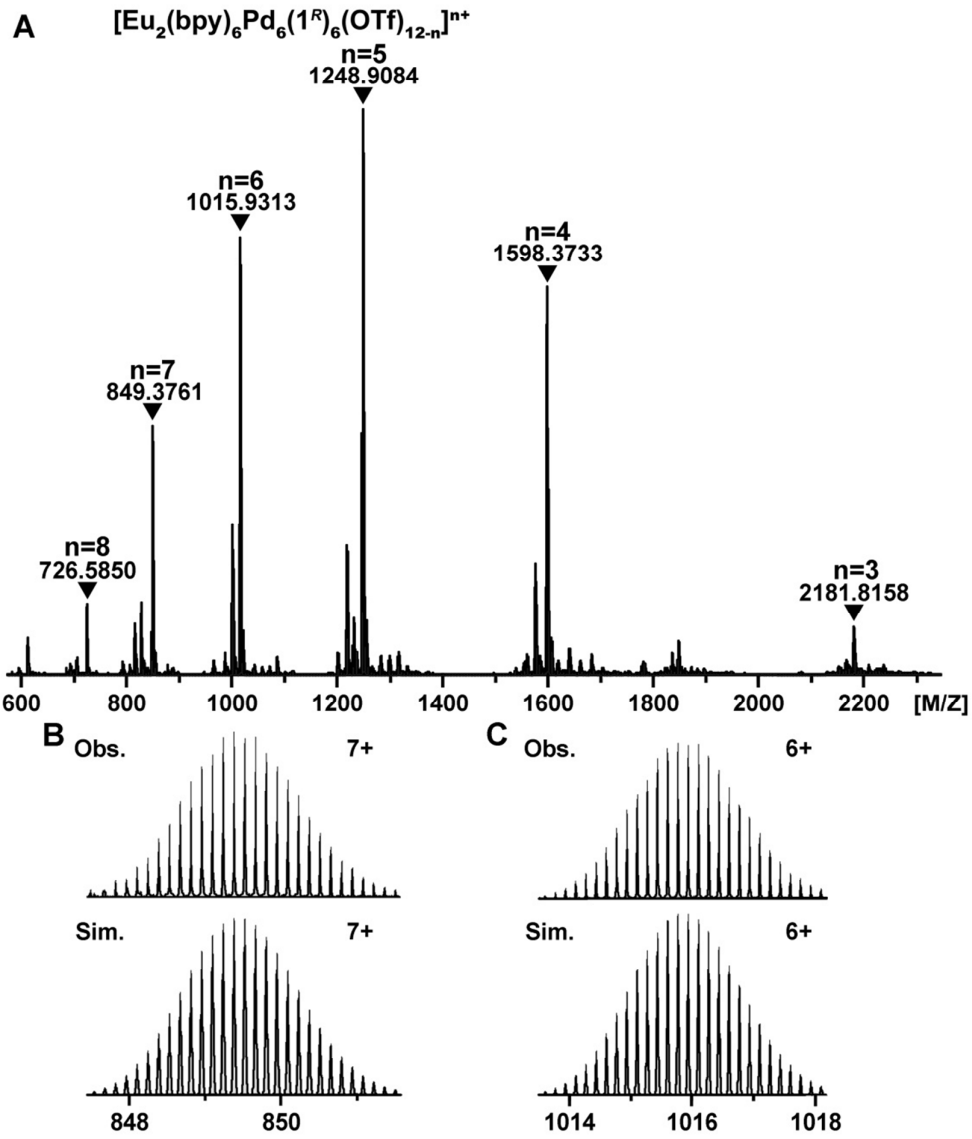

Figure S25. The ESI-TOF-MS spectra of $\mathbf{3}^{R}$-Eu with the observed and simulated isotopic patterns of the peaks corresponding to $[Eu_2(bpy)_6Pd_6(\mathbf{1}^{R})_6(OTf)_5]^{7+}$ and $[Eu_2(bpy)_6Pd_6(\mathbf{1}^{R})_6(OTf)_6]^{6+}$, respectively.

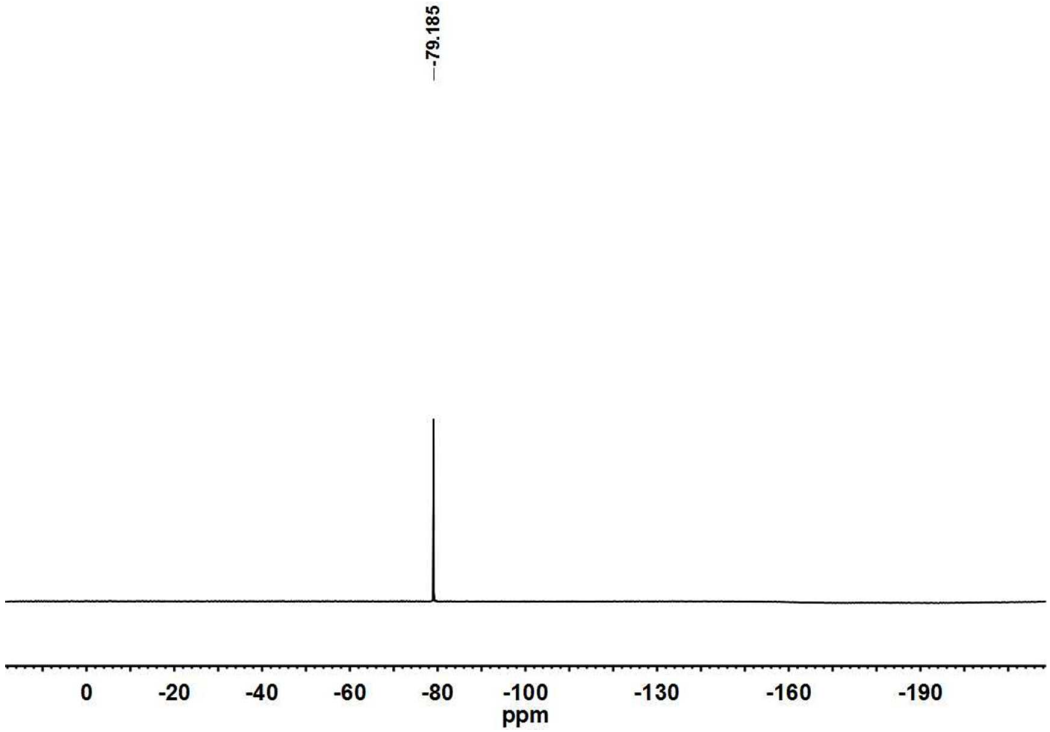

Figure S26**.** ^{19}F NMR spectrum of **3**^{R}-Eu (400 M Hz, CD_3CN, 298 K).

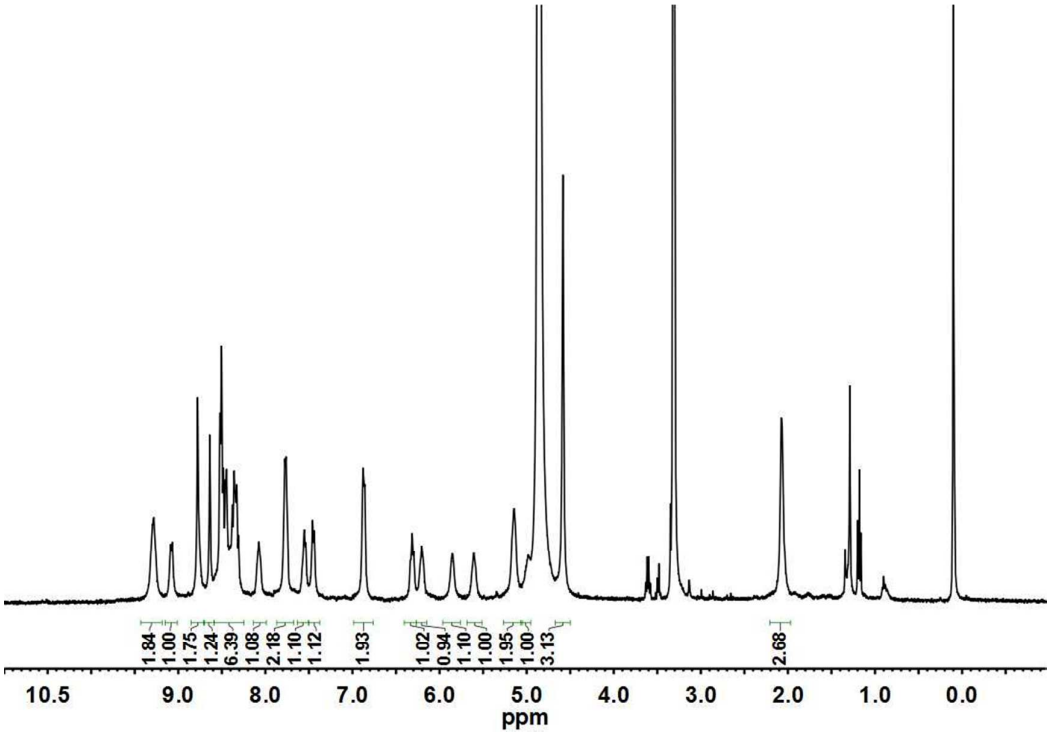

Figure S27. ^{1}H NMR spectra of **3**^{R}-Eu (400 MHz, CD_3OD, 298 K).

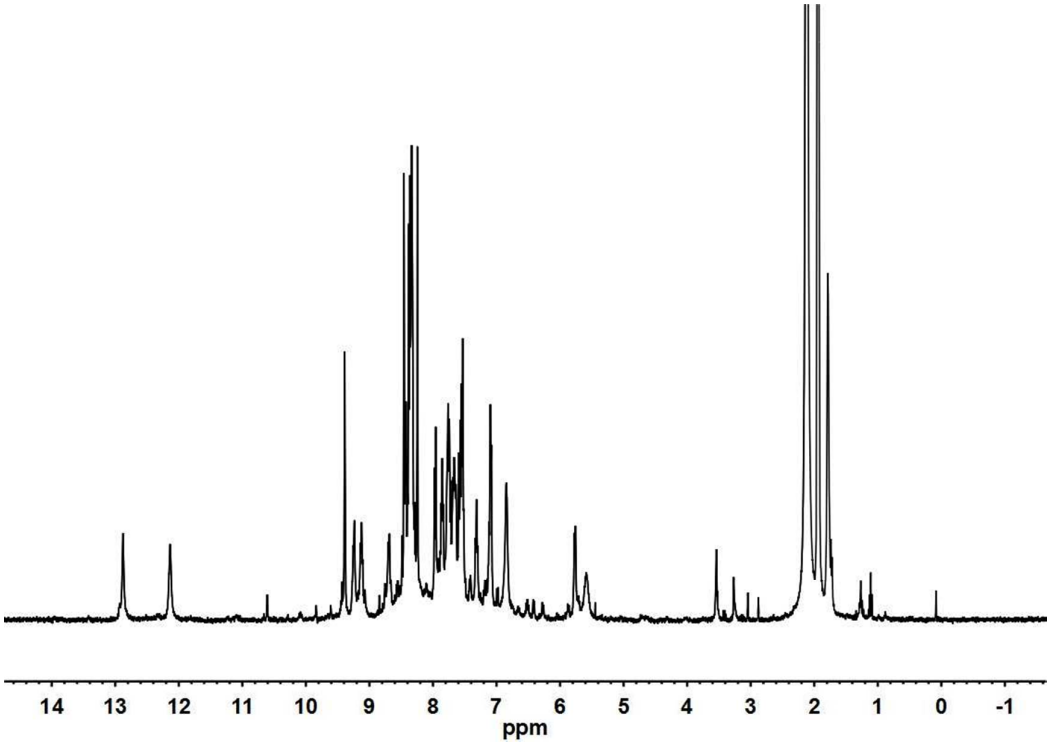

Figure S28. ^{1}H NMR spectra of **3**^{R}-Nd (400 MHz, CD_3CN, 298 K).

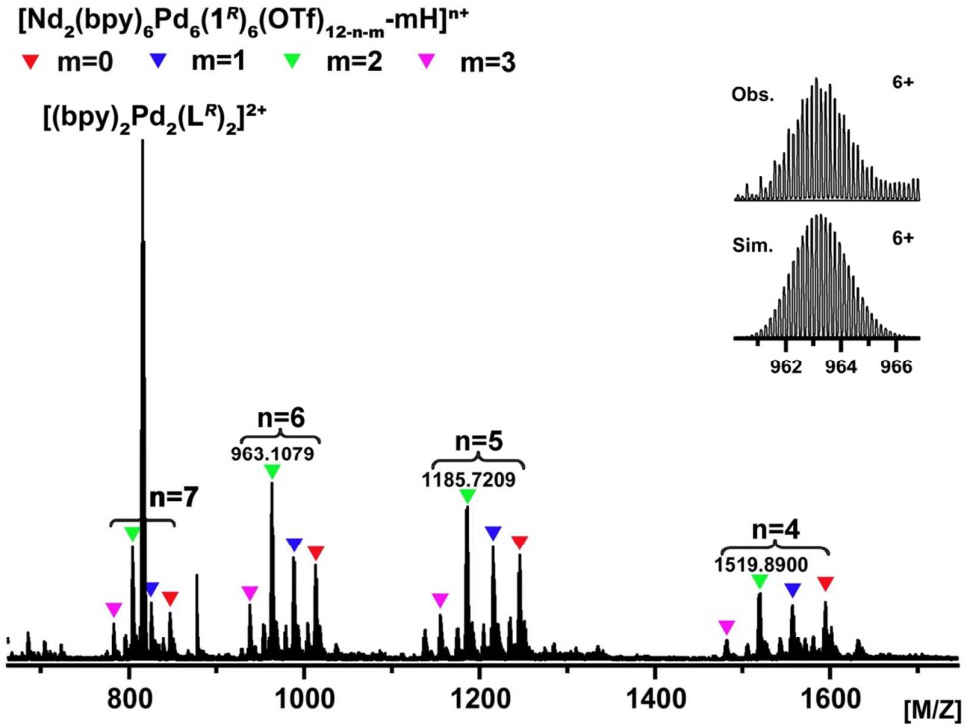

Figure S29. The ESI-TOF-MS spectra of **3**^{R}-Nd with the observed and simulated isotopic patterns of the peaks corresponding to $[Nd_2(bpy)_6Pd_6(\mathbf{1}^{R})_6(OTf)_4\text{-}2H]^{6+}$.

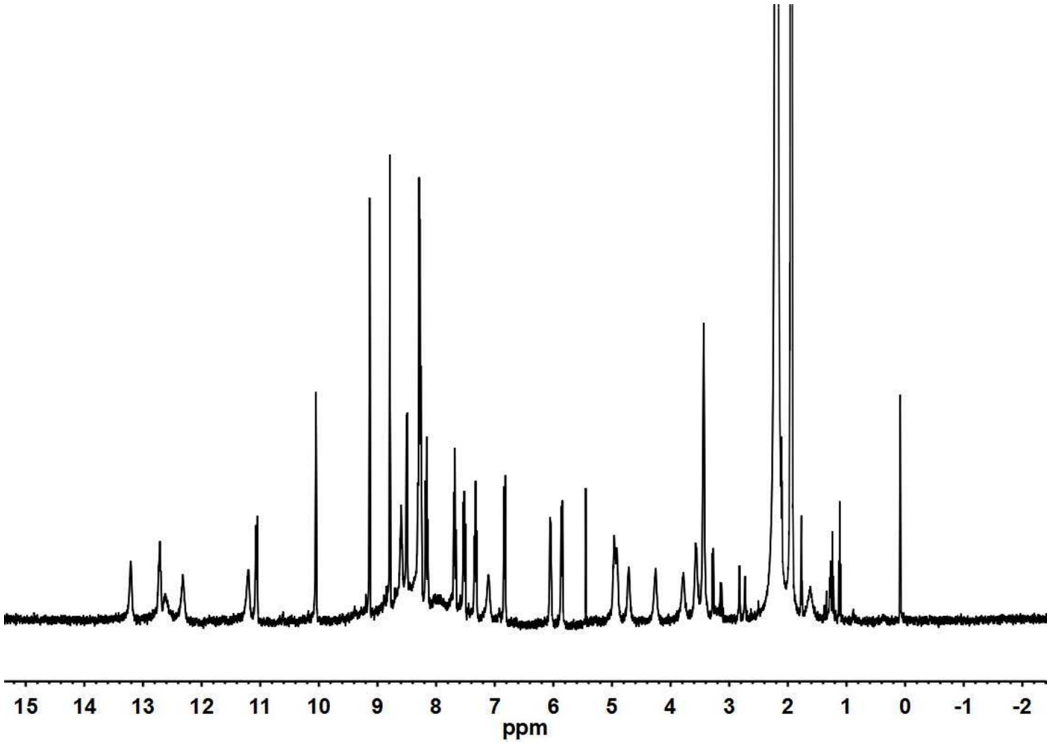

Figure S30. ^{1}H NMR spectra of $\mathbf{3}^{R}$-Yb (400 MHz, CD_3CN, 298 K).

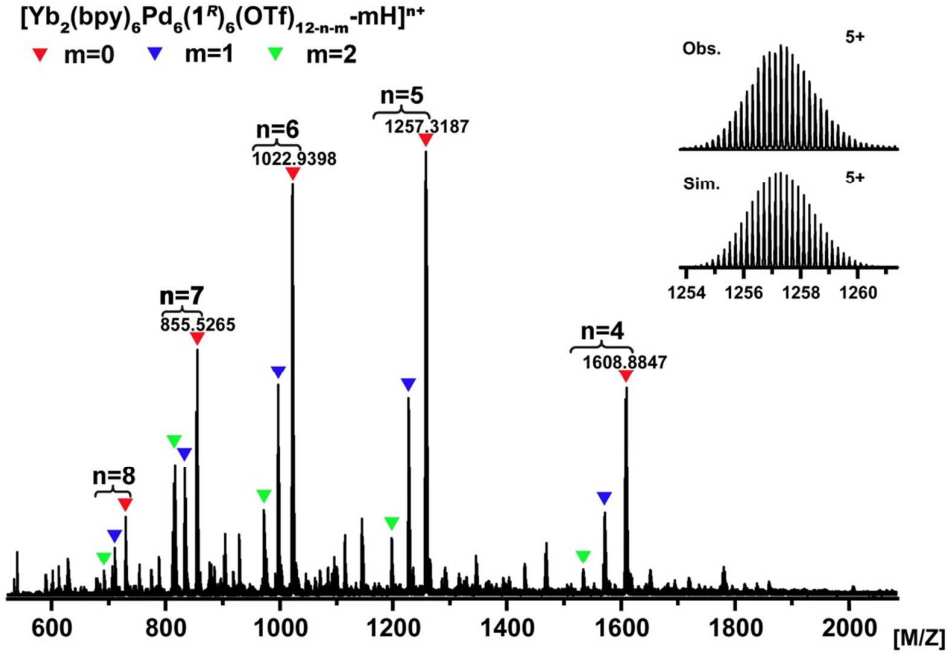

Figure S31. The ESI-TOF-MS spectra of $\mathbf{3}^{R}$-Yb with the observed and simulated isotopic patterns of the peaks corresponding to $[Yb_2(bpy)_6Pd_6(\mathbf{1}^{R})_6(OTf)_7]^{5+}$.

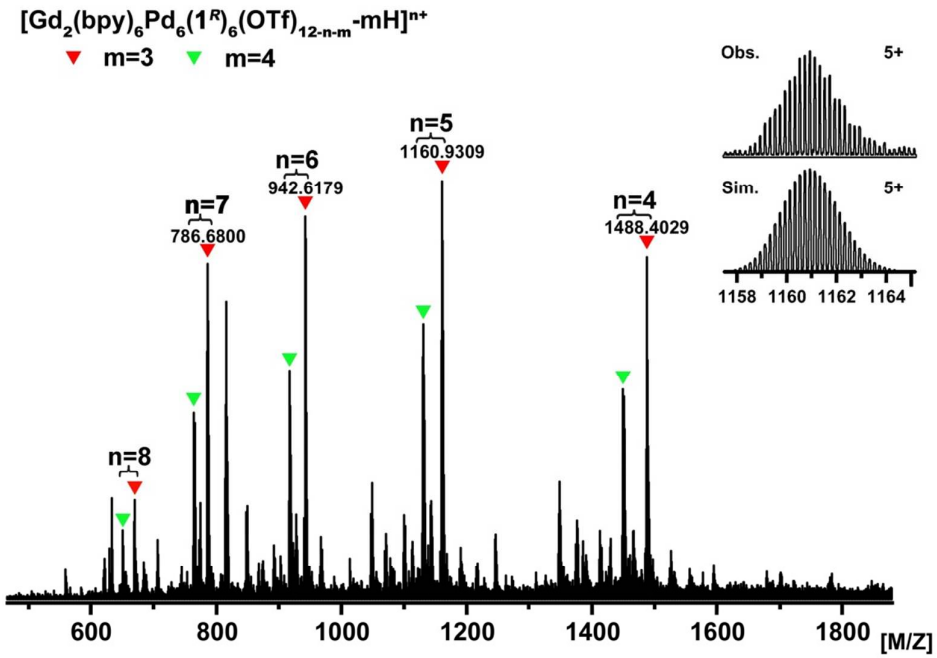

Figure S32. The ESI-TOF-MS spectra of $\mathbf{3}^{R}$-Gd with the observed and simulated isotopic patterns of the peaks corresponding to $[Gd_2(bpy)_6Pd_6(\mathbf{1}^{R})_6(OTf)_4\text{-}3H]^{5+}$.

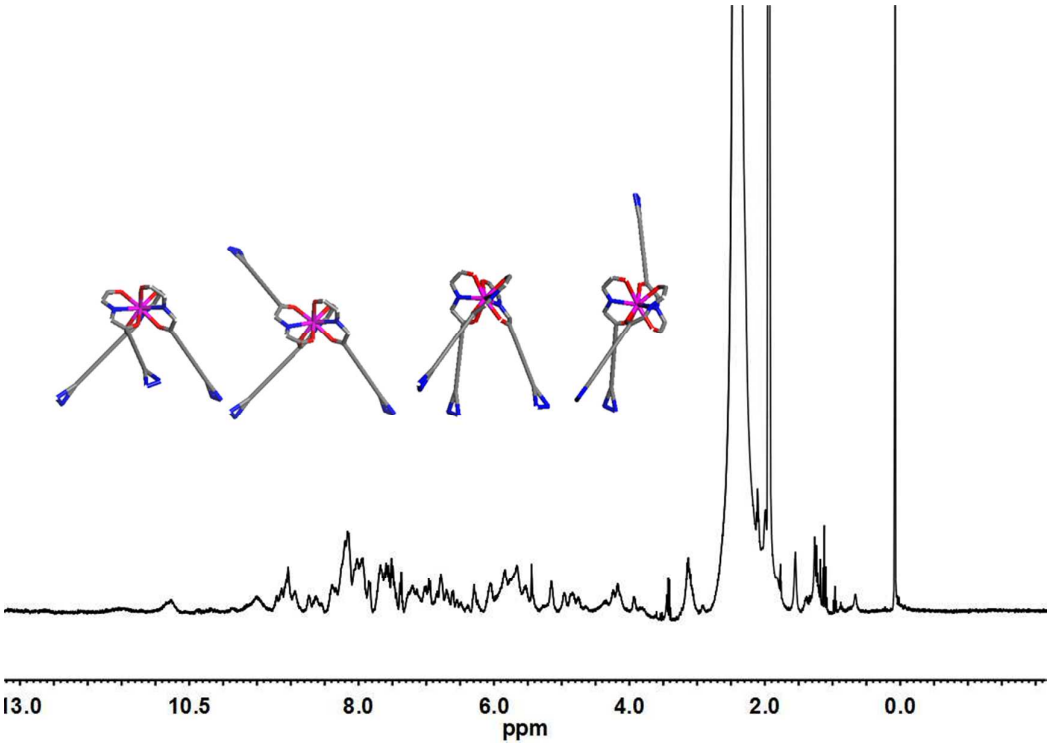

Figure S33. ^{1}H NMR spectra of $\mathbf{4}^{R}$-Eu (400 MHz, CD_3CN, 298 K).

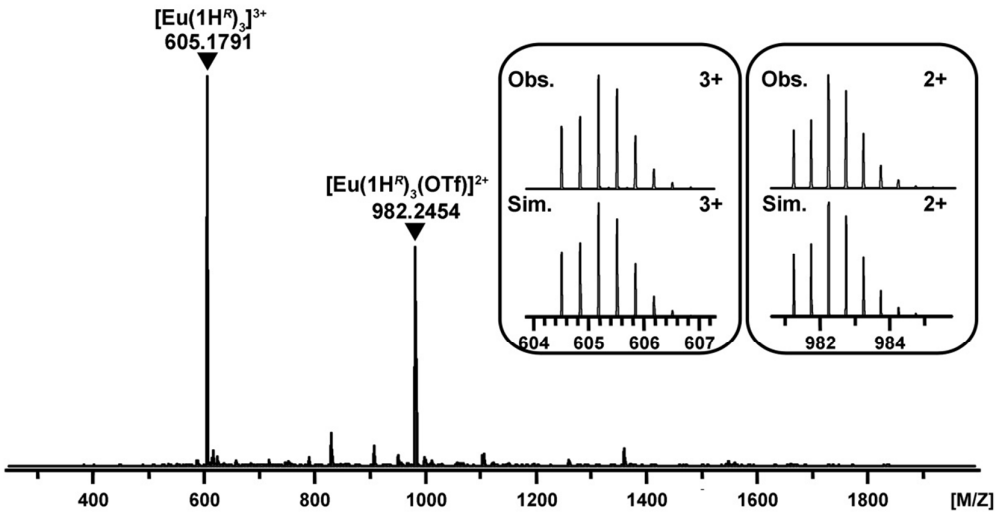

Figure S34. The ESI-TOF-MS spectra of $\mathbf{4}^{R}$-Eu with the observed and simulated isotopic patterns of the peaks corresponding to $[Eu(\mathbf{1H}^{R})_3]^{3+}$ and $[Eu(\mathbf{1H}^{R})_3(OTf)]^{2+}$, respectively.

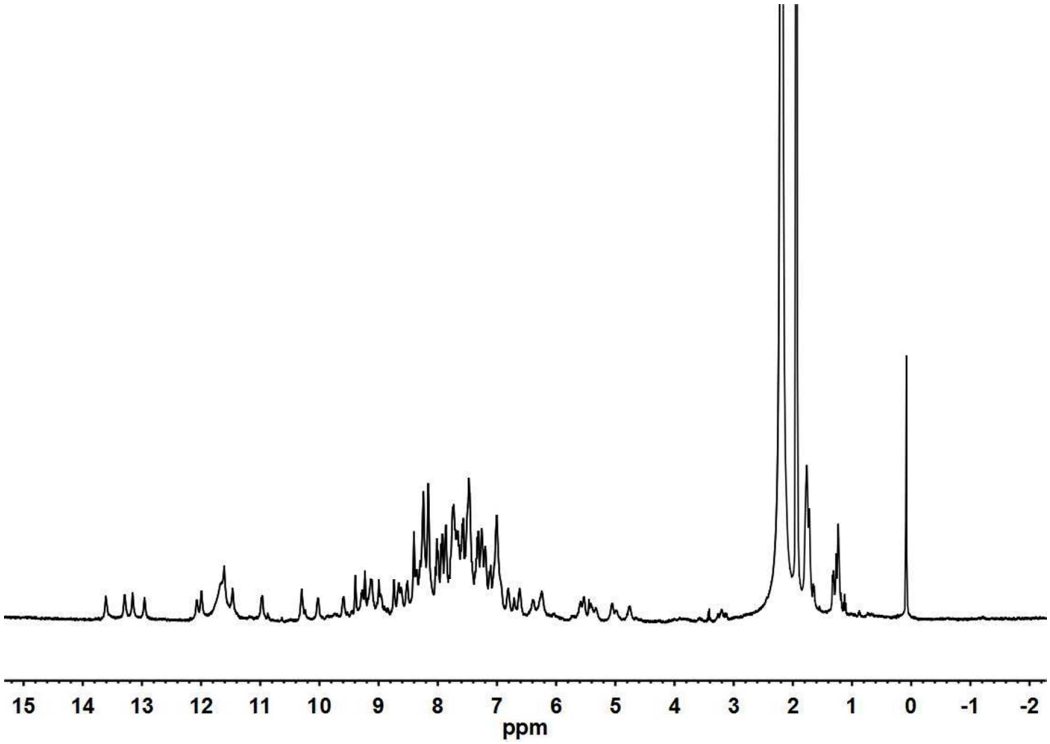

Figure S35. ^{1}H NMR spectra of $\mathbf{4}^{R}$-Nd (400 MHz, CD_3CN, 298 K).

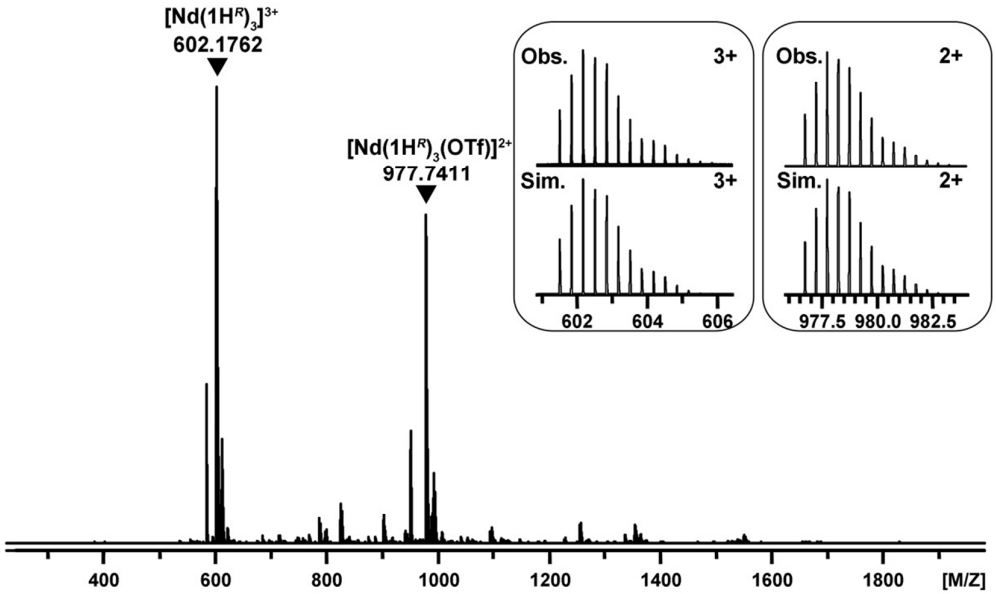

Figure S36. The ESI-TOF-MS spectra of $\mathbf{4}^{R}$-Nd with the observed and simulated isotopic patterns of the peaks corresponding to $[Nd(\mathbf{1H}^{R})_3]^{3+}$ and $[Nd(\mathbf{1H}^{R})_3(OTf)]^{2+}$, respectively.

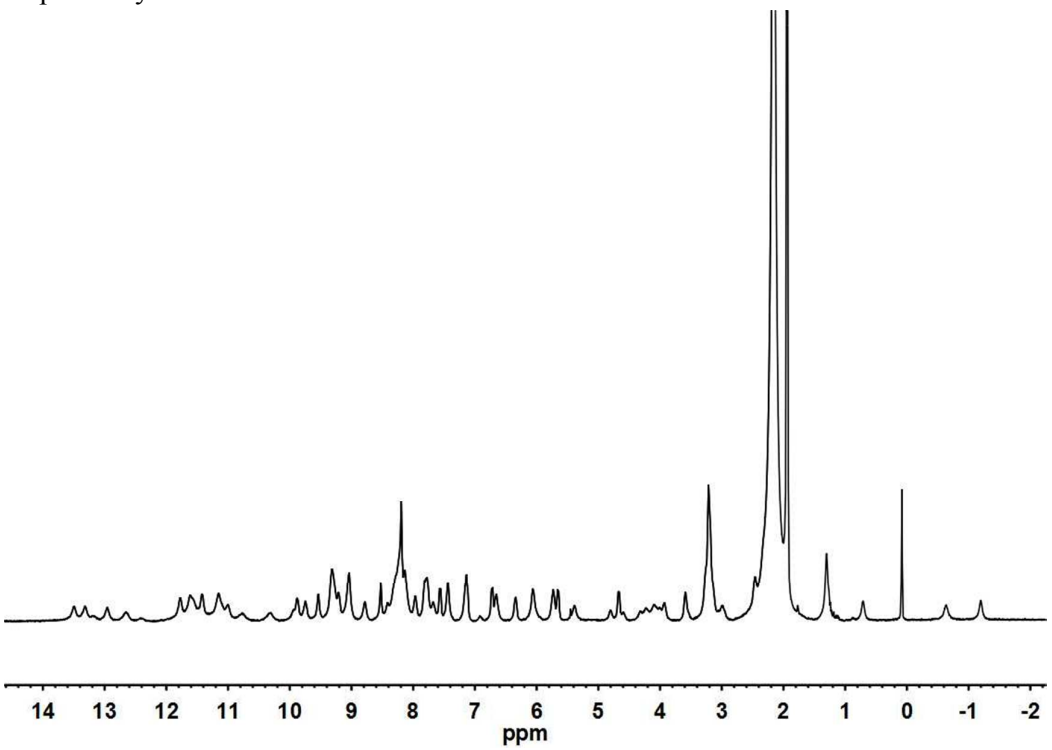

Figure S37. ^{1}H NMR spectra of $\mathbf{4}^{R}$-Yb (400 MHz, CD_3CN, 298 K).

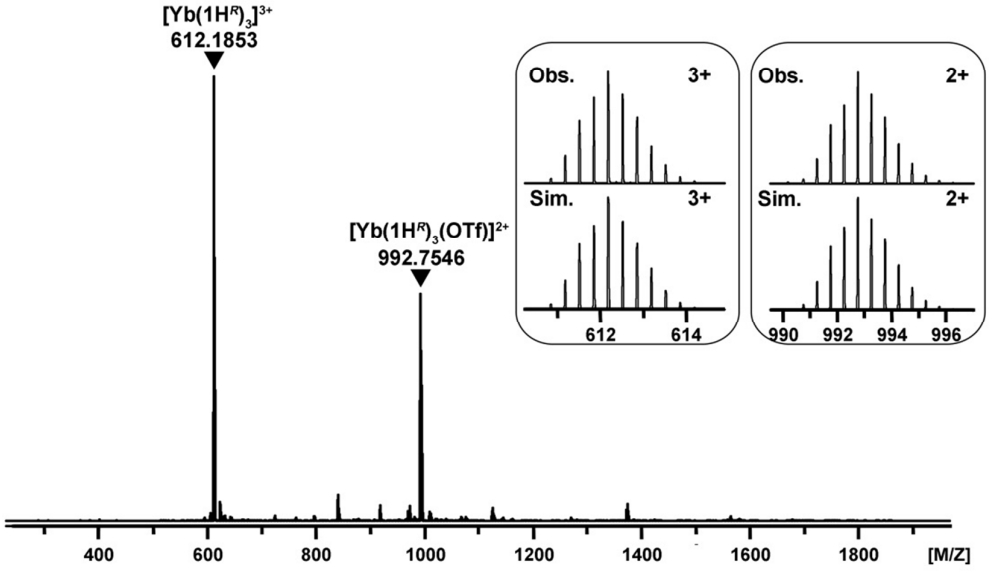

Figure S38. The ESI-TOF-MS spectra of $\mathbf{4}^{R}$-Yb with the observed and simulated isotopic patterns of the peaks corresponding to $[Yb(\mathbf{1H}^{R})_3]^{3+}$ and $[Yb(\mathbf{1H}^{R})_3(OTf)]^{2+}$, respectively.

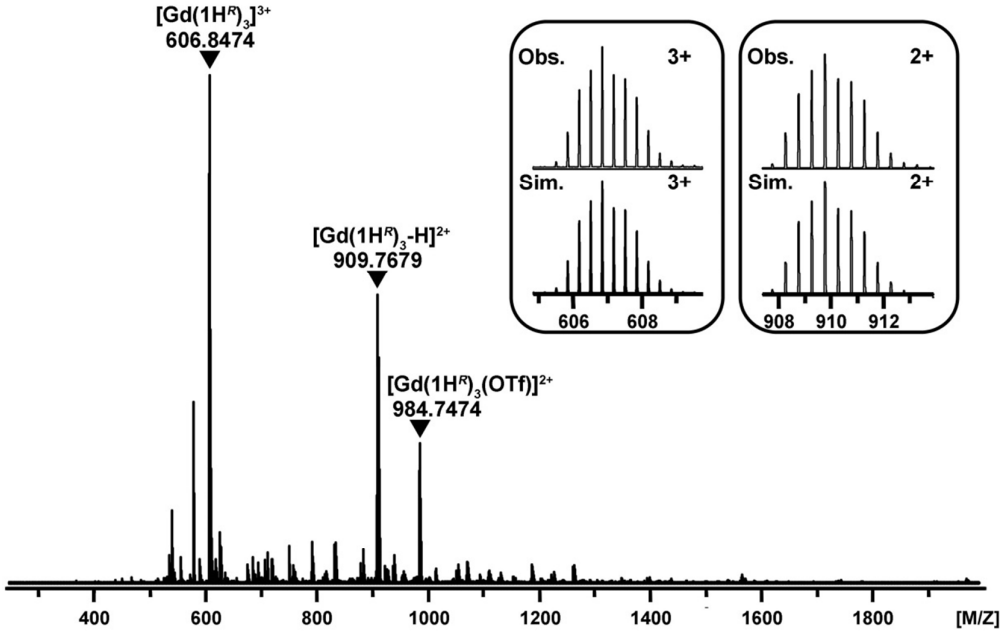

Figure S39. The ESI-TOF-MS spectra of $\mathbf{4}^{R}$-Gd with the observed and simulated isotopic patterns of the peaks corresponding to $[Gd(\mathbf{1H}^{R})_3]^{3+}$ and $[Gd(\mathbf{1H}^{R})_3\text{-H}]^{2+}$, respectively.

2. Single crystal X-ray diffraction studies

Table S1. Crystal data and structure refinement for $\mathbf{3}^{R}$-Eu.

Identification code	i213_sq	
Empirical formula	C261 H198 Eu2 F9 N48 O27 Pd6 S3	
Formula weight	5648.16	
Temperature	293(2) K	
Wavelength	1.54178 Å	
Crystal system	Cubic	
Space group	$I2_13$	
Unit cell dimensions	a = 49.4585(4) Å	α= 90°.
	b = 49.4585(4) Å	β= 90°.
	c = 49.4585(4) Å	γ = 90°.
Volume	120983(3) $Å^3$	
Z	8	
Density (calculated)	0.620 Mg/m^3	
Absorption coefficient	3.053 mm^{-1}	
F(000)	22776	
Crystal size	0.120 x 0.120 x 0.100 mm^3	
Theta range for data collection	3.575 to 61.816°.	
Index ranges	-33<=h<=39, -23<=k<=54, -46<=l<=56	
Reflections collected	66753	
Independent reflections	30983 [R(int) = 0.0809]	
Completeness to theta = 61.816°	99.1 %	
Absorption correction	Semi-empirical from equivalents	
Max. and min. transmission	1.00000 and 0.78410	
Refinement method	Full-matrix least-squares on F^2	
Data / restraints / parameters	30983 / 1993 / 1071	
Goodness-of-fit on F^2	0.835	
Final R indices [I>2sigma(I)]	R1 = 0.0628, wR2 = 0.1640	
R indices (all data)	R1 = 0.2116, wR2 = 0.2677	
Absolute structure parameter	0.065(6)	
Extinction coefficient	n/a	
Largest diff. peak and hole	0.212 and -0.141 $e.Å^{-3}$	

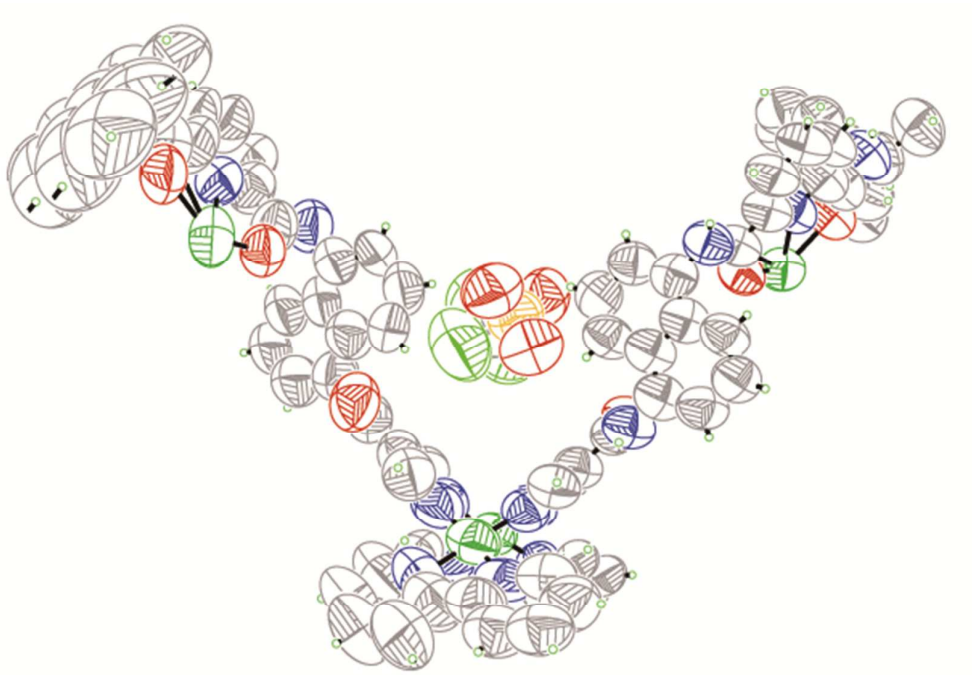

Figure S40. Ortep-drawing of the asymmetrical unit in the crystal structure of $\mathbf{3}^{R}$-Eu at 50% probability level.

3. Chiroptical Studies

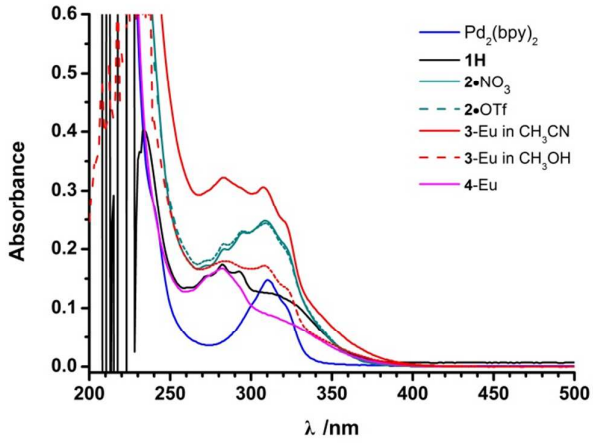

Figure S41. UV-Vis absorption spectra of $Pd_2(bpy)_2$ (1.00×10^{-5} M in CH_3CN), $\mathbf{1H}^{R}$ (1.00×10^{-5} M in DMSO), $\mathbf{2}^{R}$ (0.50×10^{-5} M in CH_3CN), $\mathbf{3}^{R}$-Eu (0.167×10^{-5} M in CH_3CN and CH_3OH), and **4**-Eu (0.33×10^{-5} M in CH_3CN) at 298K.

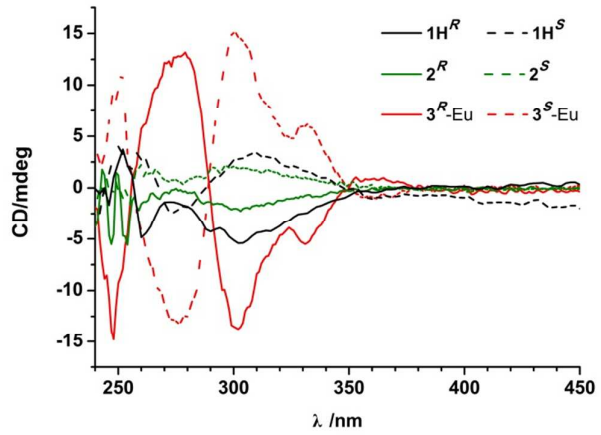

Figure S42. The circular dichroism spectra of **1H** (3.00×10^{-5} M in DMSO)**, 2**•OTf (3.00×10^{-5} M in CH_3CN) and **3**-Eu (1×10^{-5} M in CH_3CN) at room temperature.

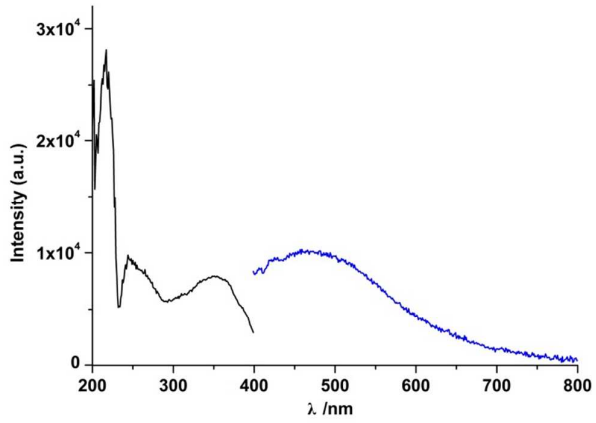

Figure S43. The excitation (black lines, λ_{em} = 470 nm) and emission (blue lines, λ_{ex} = 280 nm) spectra of **1H**^{R} (1.00×10^{-5} M, slits = 5-10) in DMSO at room temperature.

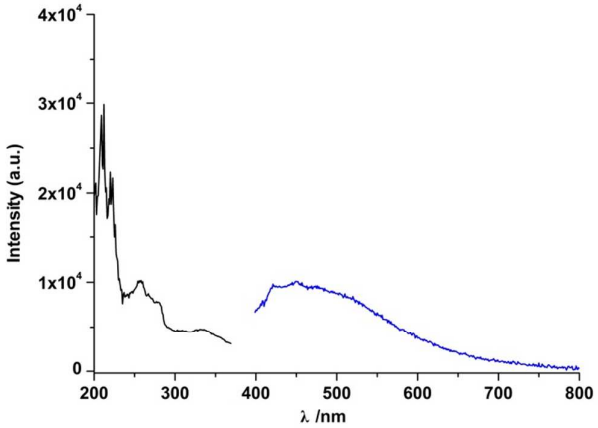

Figure S44. The excitation (black lines, λ_{em} = 440 nm) and emission (blue lines, λ_{ex} = 280 nm) spectra of **2**^{R}•NO_3 (5.00×10^{-6} M, slits = 5-10) in CH_3CN at room temperature.

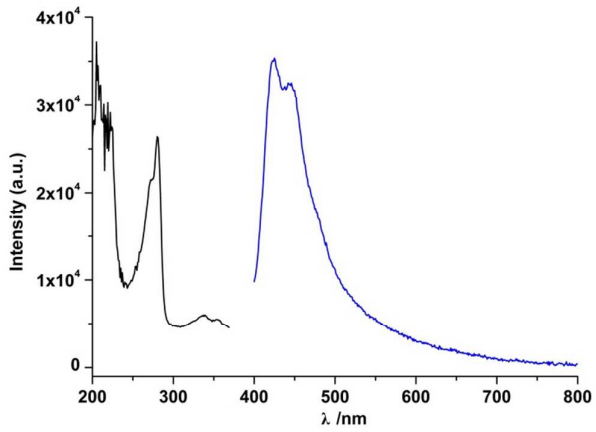

Figure S45. The excitation (black lines, λ_{em} = 440 nm) and emission (blue lines, λ_{ex} = 280 nm) spectra of **2**^{R}**•OTf** (5.00 × 10^{-6} M, slits = 5-10) in CH_3CN at room temperature.

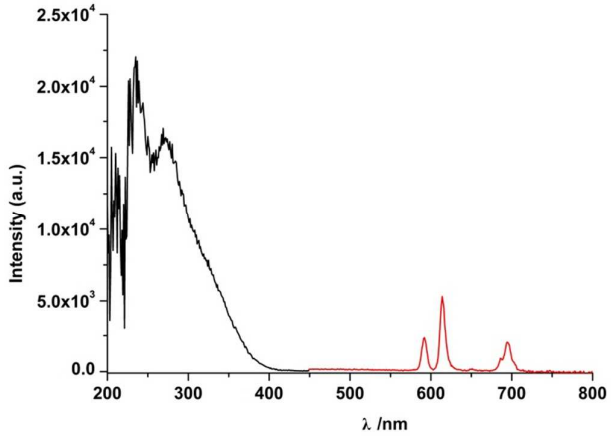

Figure S46. The excitation (black lines, λ_{em} = 615 nm) and emission (red lines, λ_{ex} = 270 nm) spectra of **4** ^{R}-Eu (3.33 × 10^{-6} M, slits = 2-5) in CH_3CN at room temperature.

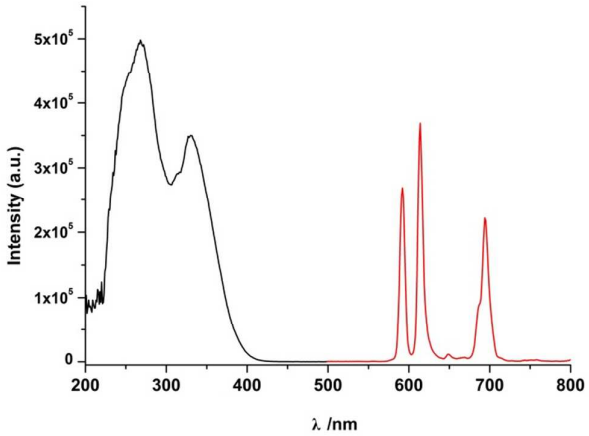

Figure S47. The excitation (black lines, λ_{em} = 615 nm) and emission (red lines, λ_{ex} = 332 nm) spectra of **3**^{R}-Eu (1.67 × 10^{-6} M, slits = 2-5) in CH_3CN at room temperature.

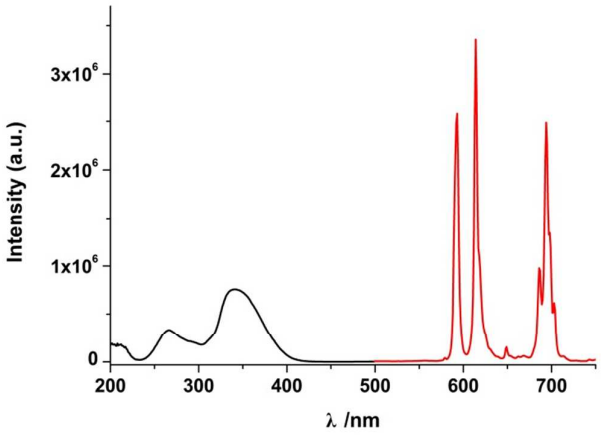

Figure S48. The excitation (black lines, λ_{em} = 615 nm) and emission (red lines, λ_{ex} = 345 nm) spectra of **3**^{R}-Eu (2.0×10^{-5} M, slits = 2-8) in CH_3OH at room temperature.

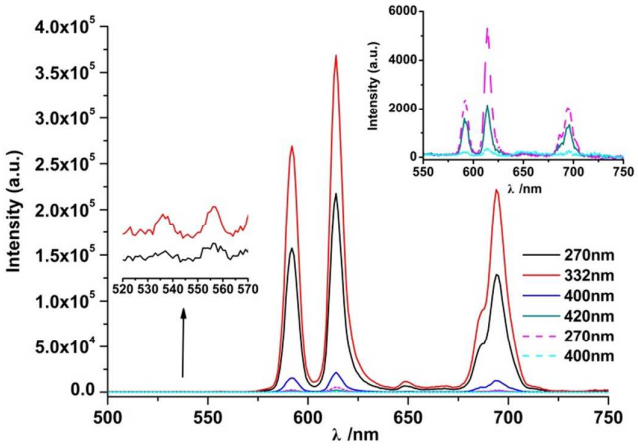

Figure S49. The emission spectra of **4**^{R}-Eu (dashed lines, 3.33×10^{-6} M) and **3**^{R}-Eu (solid lines, 1.67×10^{-6} M) using different excitation wavelengths from 270 to 420 nm (inset is the partial enlarged views) (slits = 2-5 nm, in CH_3CN).

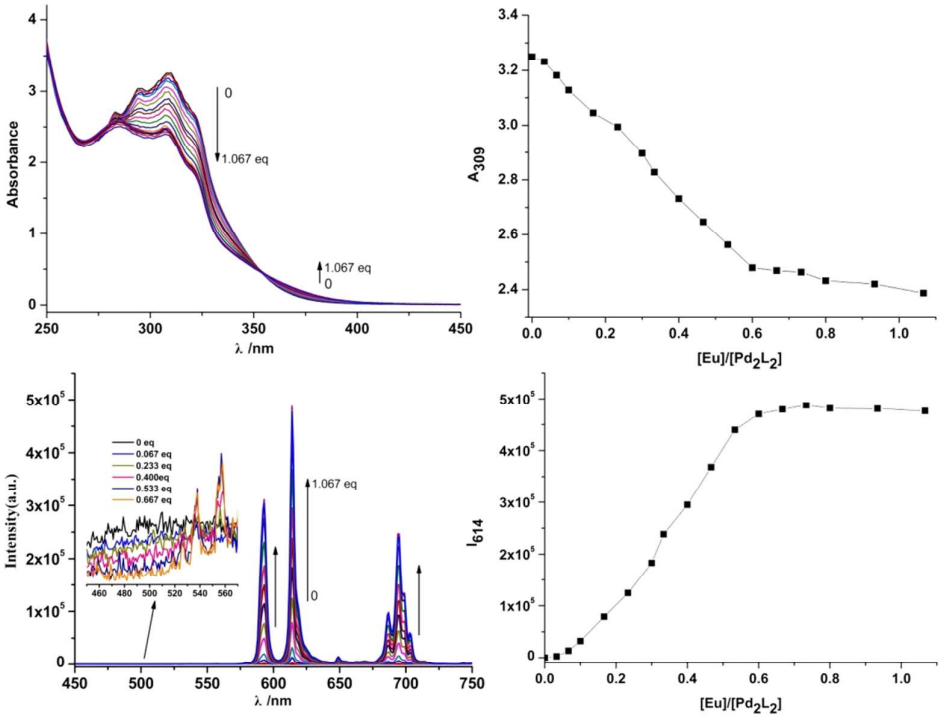

Figure S50. A) UV-vis absorption spectra of titrating $\mathbf{2}^{R}$•**OTf** with $Eu(OTf)_3$. B) Absorbance variation with the addition of different amount of $Eu(OTf)_3$ at 309 nm. C) Luminescence emission spectra of titrating $\mathbf{2}^{R}$•**OTf** with $Eu(OTf)_3$. D) Luminescence emission intensity variation with the addition of different amount of $Eu(OTf)_3$ at 614nm. ([$\mathbf{2}^{R}$•**OTf**] = 3×10^{-5} M in CH_3CN, λ_{ex} = 337 nm).

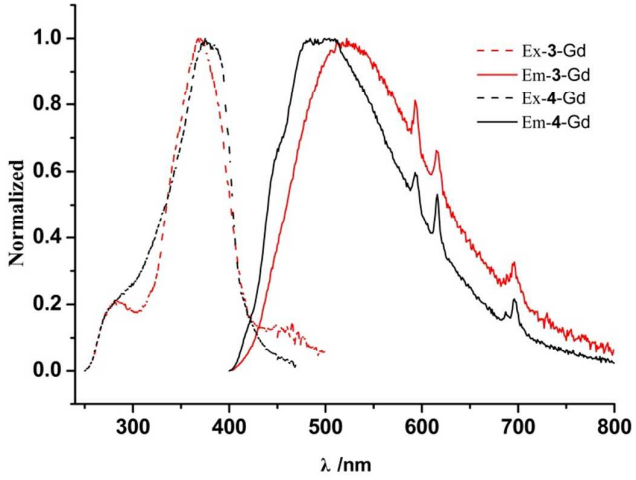

Figure S51. The excitation and emission spectra of $\mathbf{4}^{R}$-Gd (solid, λ_{em} = 500 nm, λ_{ex} = 370 nm, 1.67×10^{-6} M, slits = 4-8) and $\mathbf{3}^{R}$-Gd (solid, λ_{em} = 520 nm, λ_{ex} = 370 nm, 1.67×10^{-6} M, slits = 4-8) at 77K.

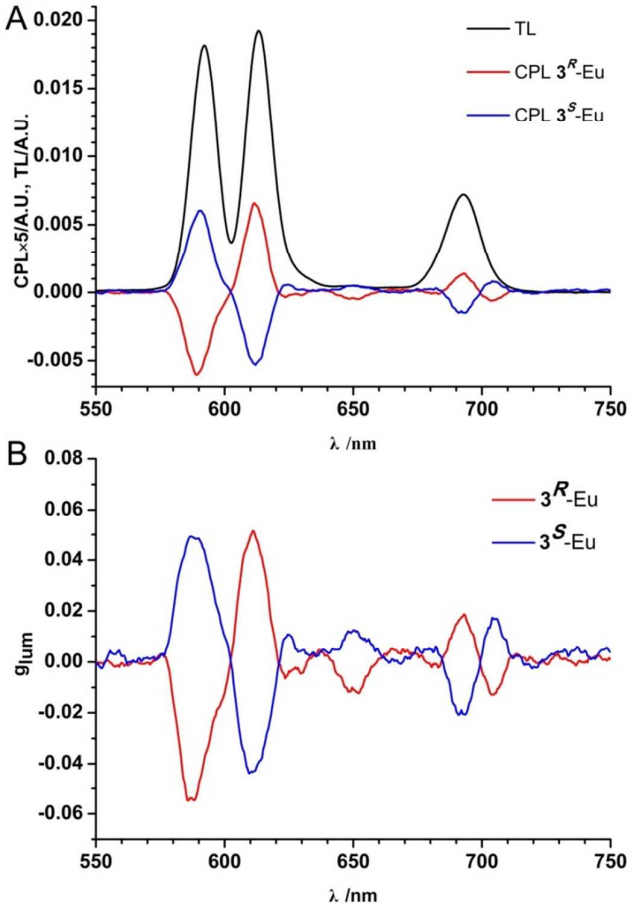

Figure S52. Circularly polarized luminescence spectra of both enantiomers and total luminescence spectra of **3**-Eu (2×10^{-5} M，λ_{ex} = 350 nm) in CH_3CN.

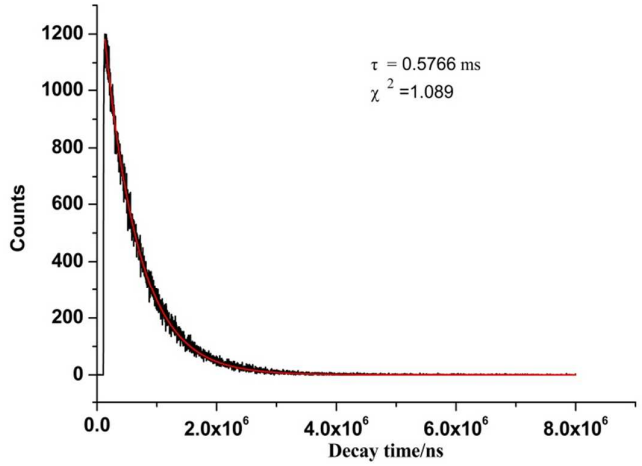

Figure S53. Excitated state decay curve(black line) with mono exponential fit (red line) of **3** ^{R}-Eu (3×10^{-5} M in CD_3OD, λ_{ex} = 350 nm, λ_{em} = 615 nm).

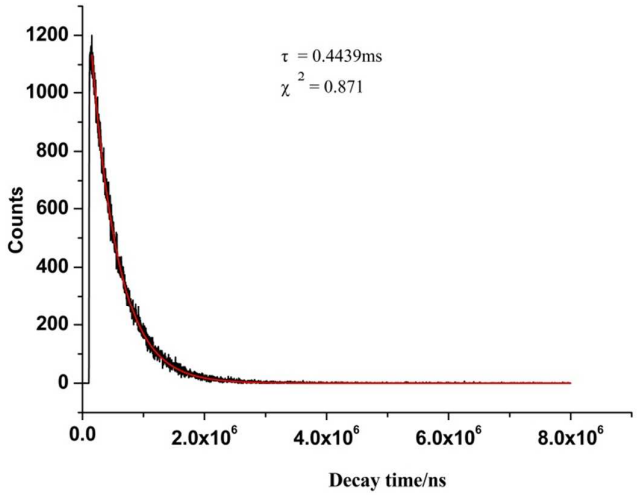

Figure S54. Excited state decay curve (black line) with mono exponential fit (red line) of **3** ^{R}-Eu (3×10^{-5} M in CH_3OH, λ_{ex} = 350 nm, λ_{em} = 615 nm).

The calculation of **number of Coordinated Solvent Molecules**[S1]:

$$q=A(\tau_{methanol}^{-1} - \tau_{deutero\text{-}methanol}^{-1} - B) = 1.089$$

$$A = 2.1,\ B = 0$$

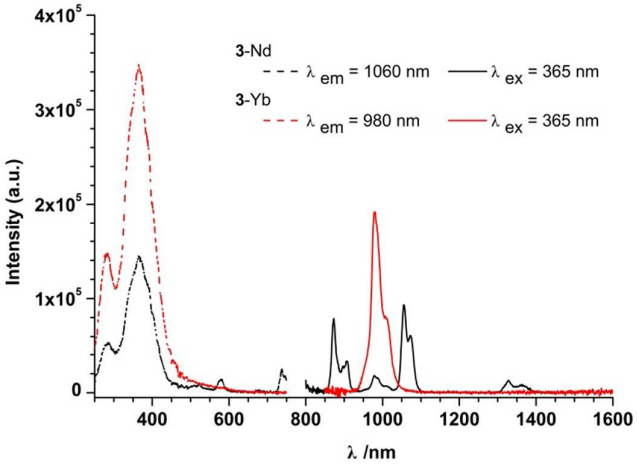

Figure S55. NIR luminescence excitation (dashed lines) and emission (solid lines) spectra of **3** ^{R}-Nd and **3** ^{R}-Yb (in solid state).

4. Detection of Antibiotics

Scheme S2. The structures of different kinds of antibiotics.

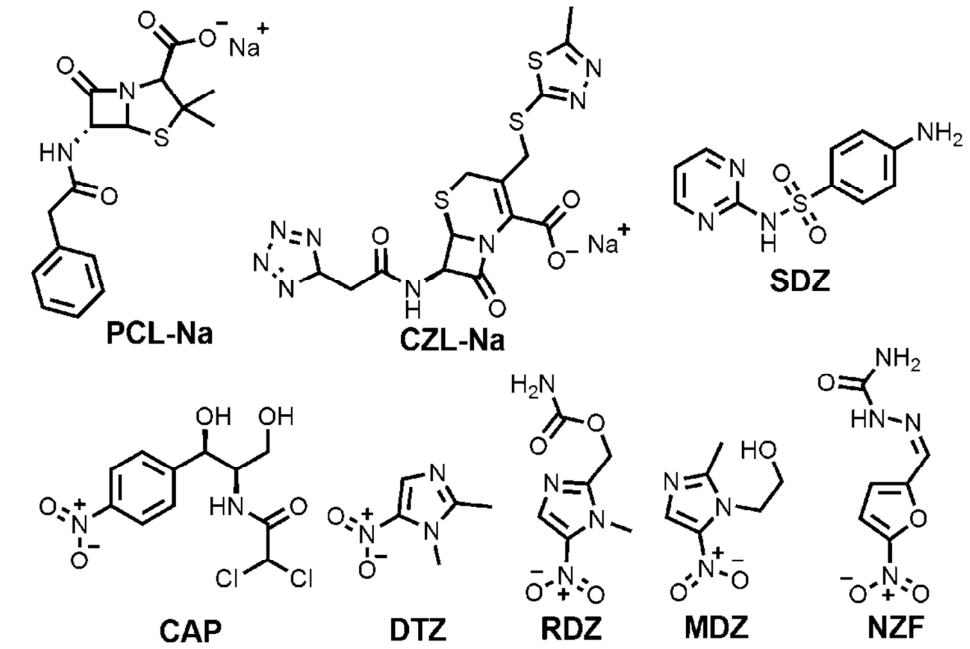

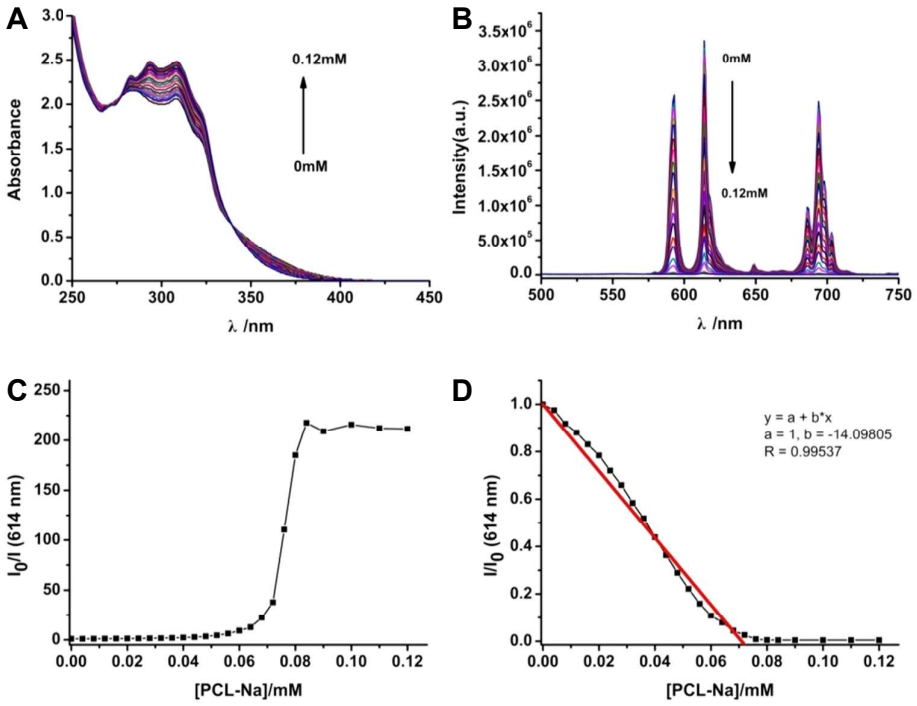

Figure S56. UV-vis absorption (A) and luminescence emission (B) spectra of titrating $\mathbf{3}^{R}$-Eu with PCL-Na; luminescence quenching efficiencies I_0/I (C) and I/I_0 (D) of $\mathbf{3}^{R}$-Eu with the addition of different amount of PCL-Na at 614 nm. ([$\mathbf{3}^{R}$-Eu] = 0.02 mM in CH_3OH, λ_{ex} = 345 nm).

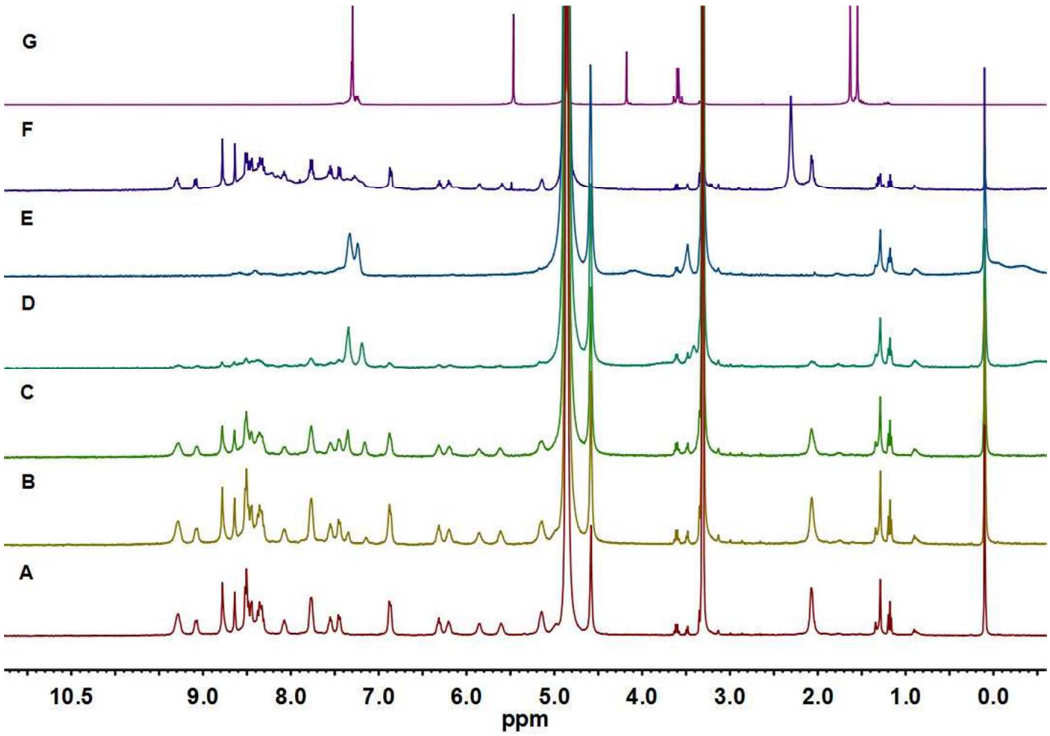

Figure S57. ^{1}H NMR spectra of titrating $\mathbf{3}^R$-Eu (0.5 mM) with PCL-Na: $\mathbf{3}^R$-Eu with the addition of A) 0 mM.; B) 0.25 mM; C) 0.5 mM; D) 1.0 mM; E) 1.5 mM PCL-Na F) further adding 0.5 mM $Eu(OTf)_3$ into E; and G) PCL-Na (400 MHz, CD_3OD, 298 K).

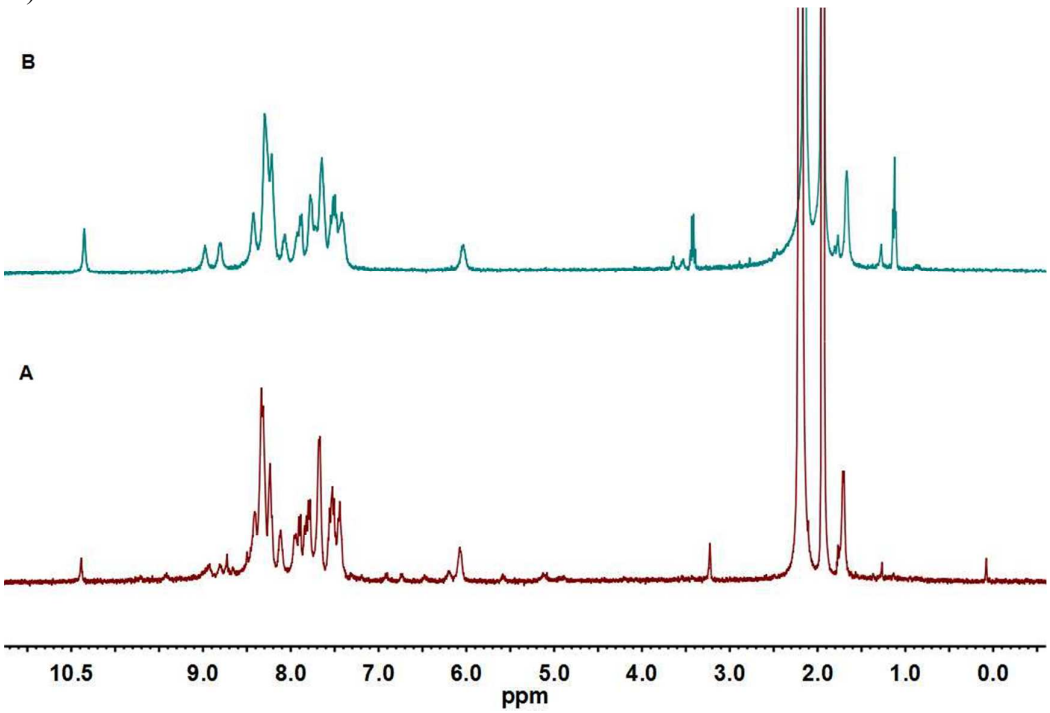

Figure S58. ^{1}H NMR spectra of A) the precipitation on adding 1.5 mM PCL-Na into the methanol solution of $\mathbf{3}^R$-Eu (0.5 mM) and B) $\mathbf{2}^R$•OTf (400 MHz, CD_3CN, 298 K).

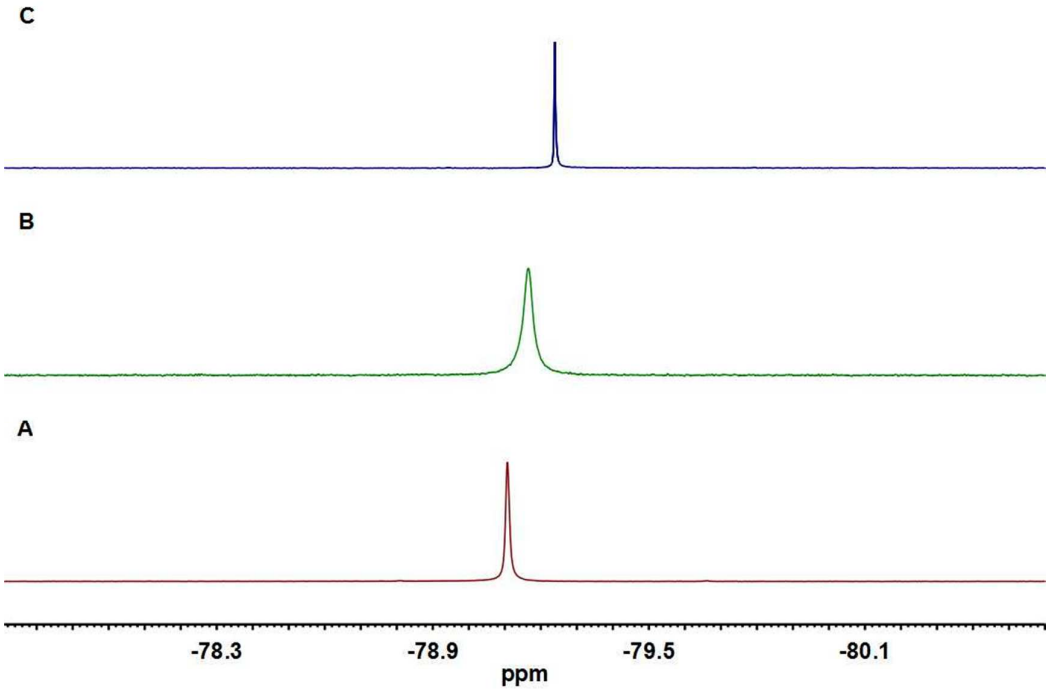

Figure S59. Partial ^{19}F NMR spectra of A) $\mathbf{3}^{R}$-Eu (0.5 mM); B) the precipitation on adding 1.5 mM PCL-Na into the methanol solution of $\mathbf{3}^{R}$-Eu (0.5 mM); C) $\mathbf{2}^{R}$•OTf (400 MHz, CD_3CN, 298 K).

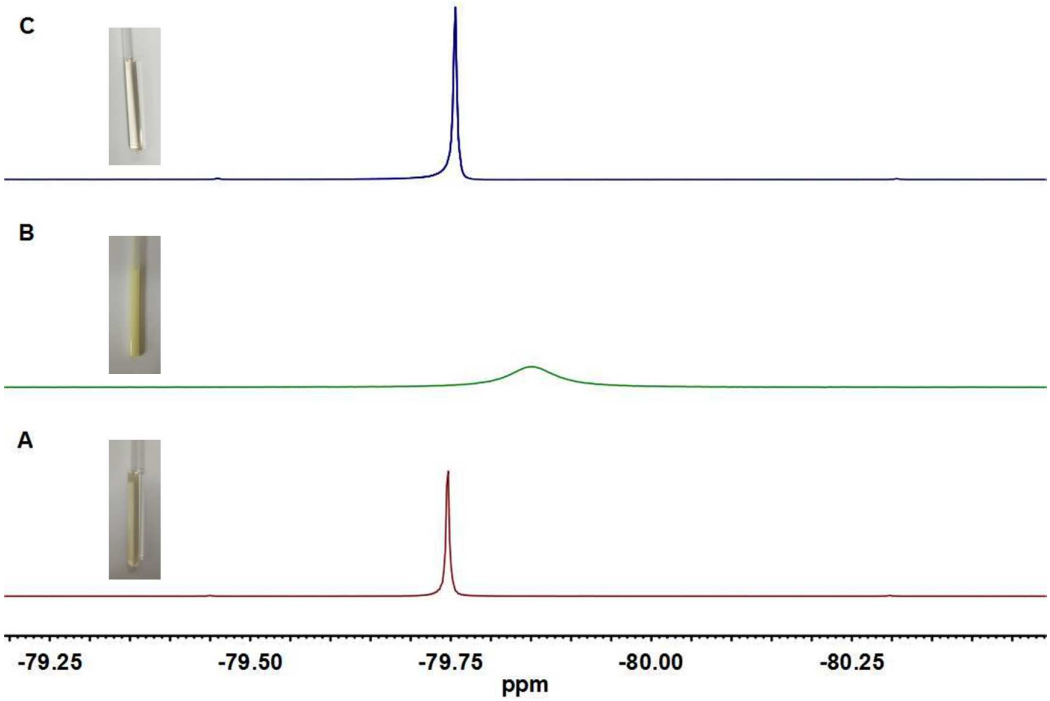

Figure S60. Partial ^{19}F NMR spectra of the solution of A) $\mathbf{3}^{R}$-Eu (0.5 mM); B) adding 1.5 mM PCL-Na into A and C) further adding 0.5 mM Eu(OTf) into B with insets showing the photographs of solution A, B and C (400 MHz, CD_3OD, 298 K).

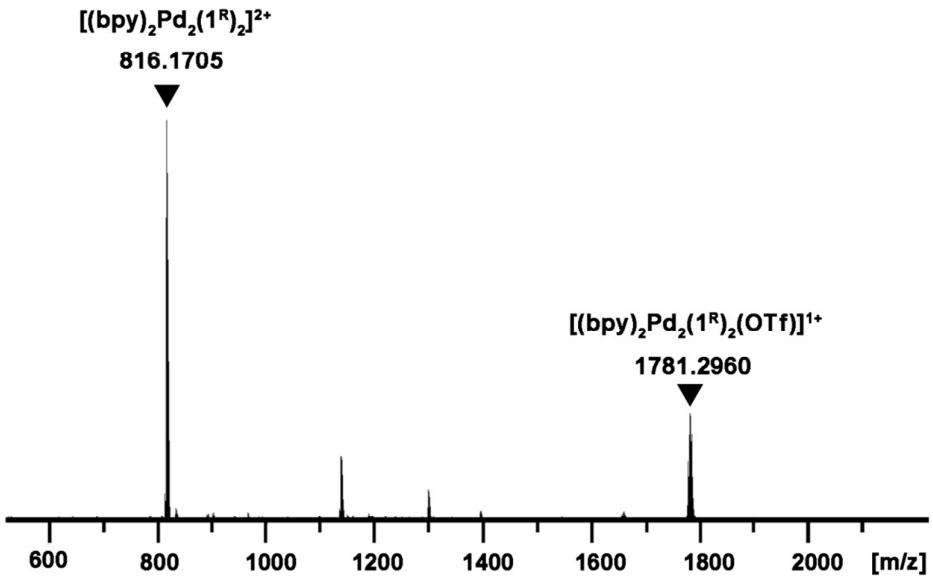

Figure S61. ESI-TOF-MS of $\mathbf{3}^{R}$-Eu after addition of 4.0 equiv PCL-Na .

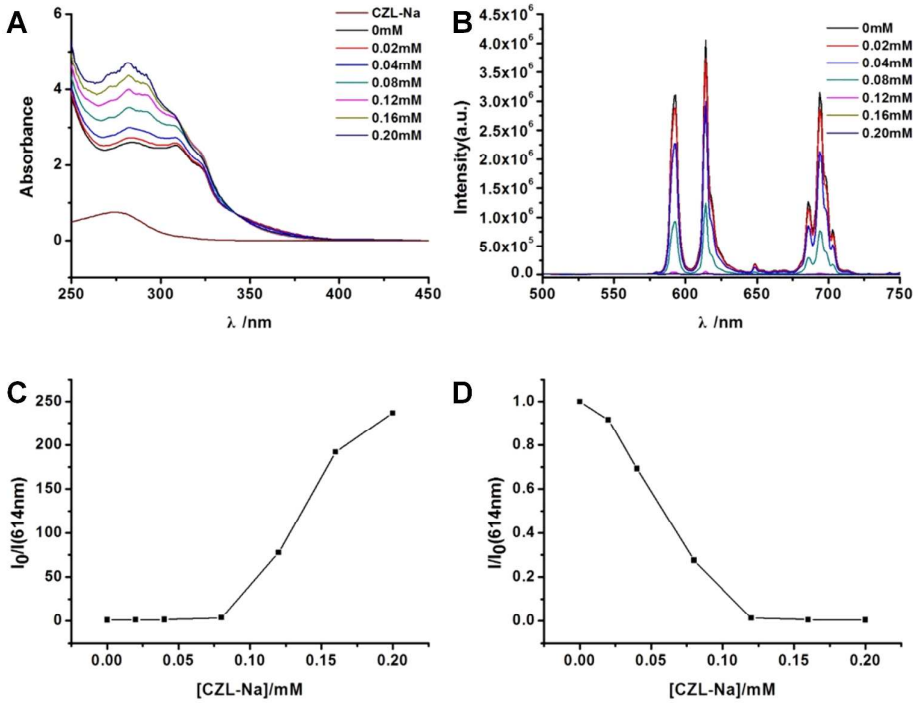

Figure S62. UV-vis absorption (A) and luminescence emission (B) spectra of titrating $\mathbf{3}^{R}$-Eu with CZL-Na; luminescence quenching efficiencies I_0/I (C) and I/I_0 (D) of $\mathbf{3}^{R}$-Eu with the addition of different amount of CZL-Na at 614 nm. ([$\mathbf{3}^{R}$-Eu] = 0.02 mM in CH_3OH, λ_{ex} = 345 nm).

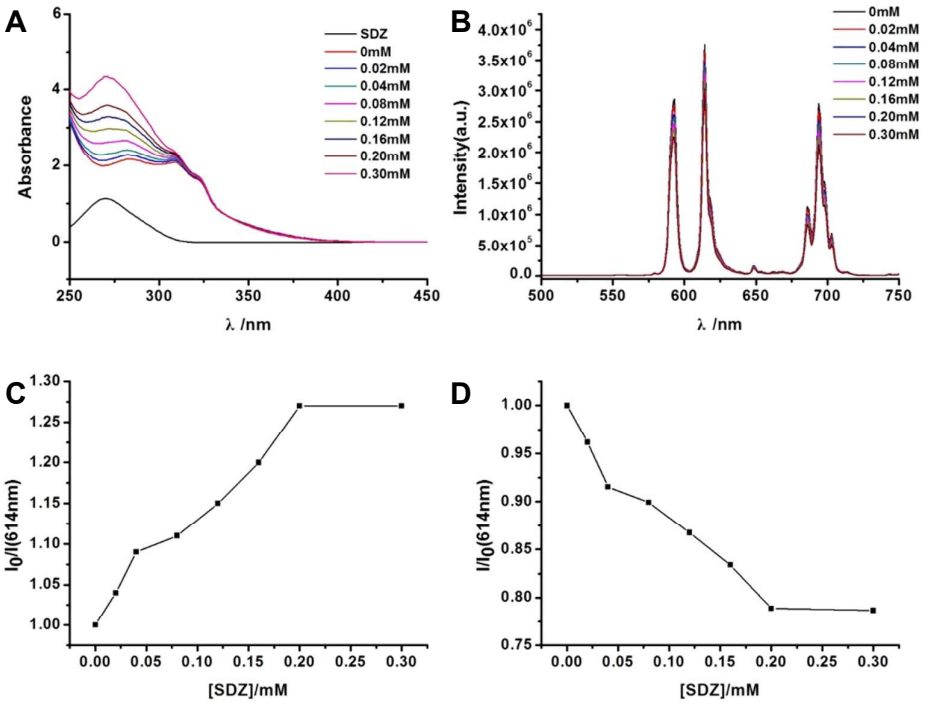

Figure S63. UV-vis absorption (A) and luminescence emission (B) spectra of titrating **3**^{R}-Eu with SDZ; luminescence quenching efficiencies I_0/I (C) and I/I_0 (D) of **3**^{R}-Eu with the addition of different amount of SDZ at 614 nm. ([**3**^{R}-Eu] = 0.02 mM in CH_3OH, λ_{ex} = 345 nm).

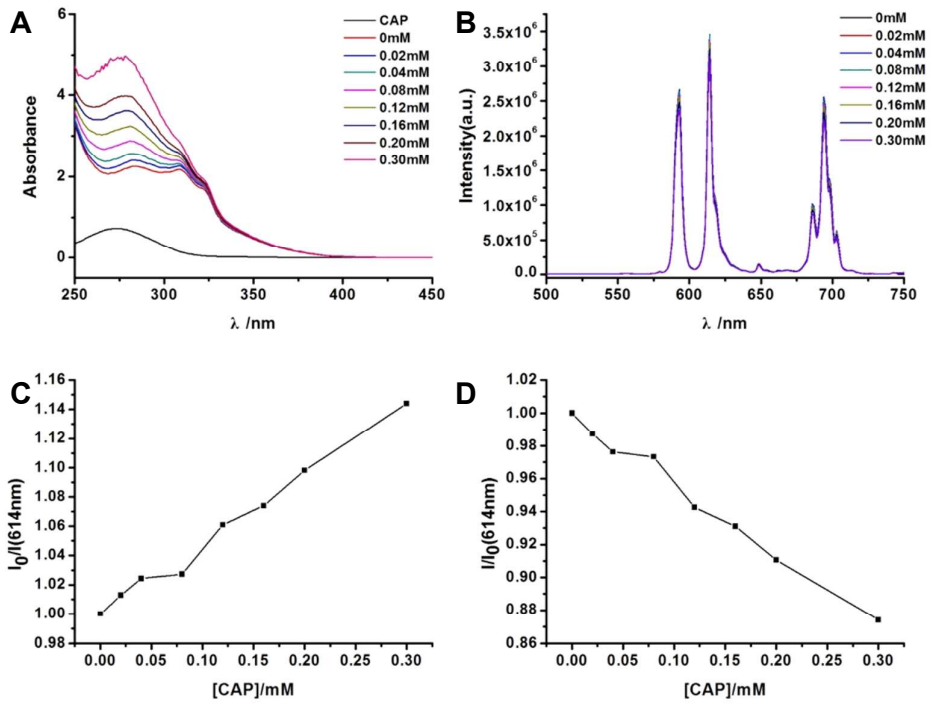

Figure S64. UV-vis absorption (A) and luminescence emission (B) spectra of titrating **3**^{R}-Eu with CAP; luminescence quenching efficiencies I_0/I (C) and I/I_0 (D) of **3**^{R}-Eu with the addition of different amount of CAP at 614 nm. ([**3**^{R}-Eu] = 0.02 mM in CH_3OH, λ_{ex} = 345 nm).

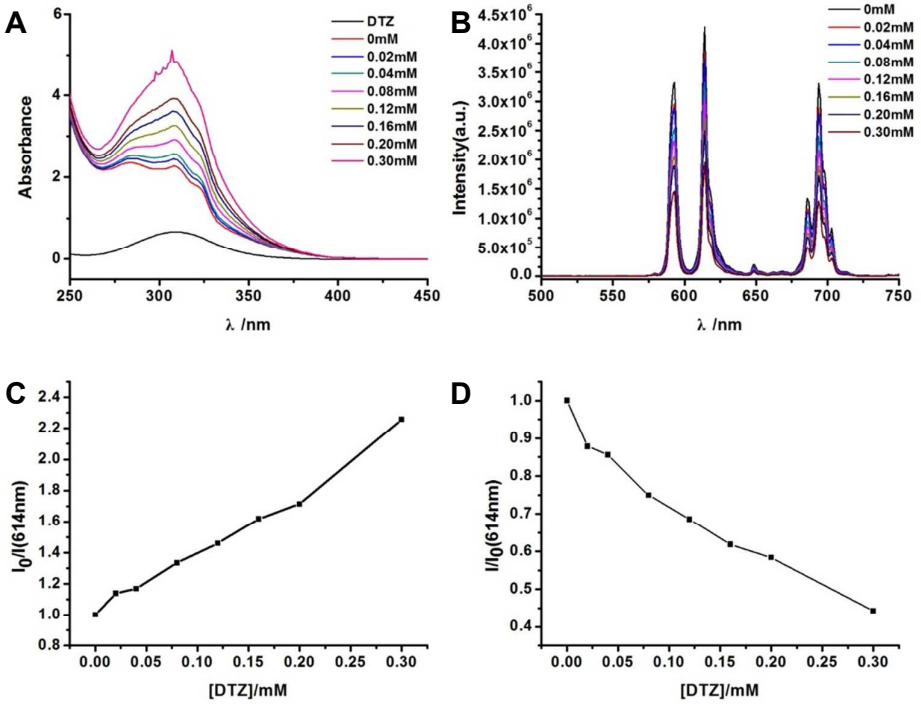

Figure S65. UV-vis absorption (A) and luminescence emission (B) spectra of titrating **3**^{R}-Eu with DTZ; luminescence quenching efficiencies I_0/I (C) and I/I_0 (D) of **3**^{R}-Eu with the addition of different amount of DTZ at 614 nm. ([**3**^{R}-Eu] = 0.02 mM in CH_3OH, λ_{ex} = 345 nm).

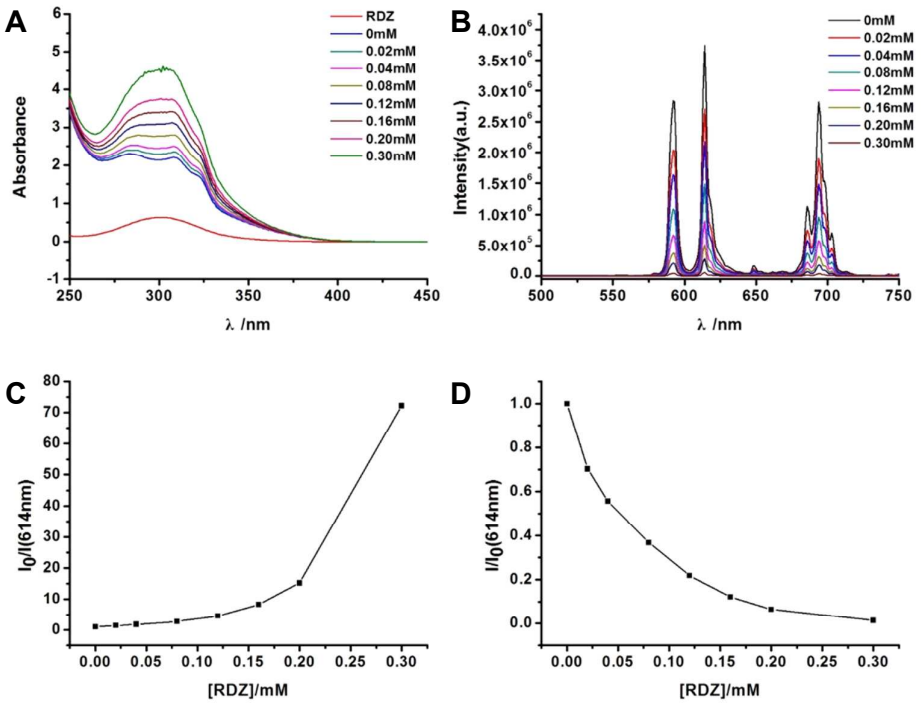

Figure S66. UV-vis absorption (A) and luminescence emission (B) spectra of titrating **3**^{R}-Eu with RDZ; luminescence quenching efficiencies I_0/I (C) and I/I_0 (D) of **3**^{R}-Eu with the addition of different amount of RDZ at 614 nm. ([**3**^{R}-Eu] = 0.02 mM in CH_3OH, λ_{ex} = 345 nm).

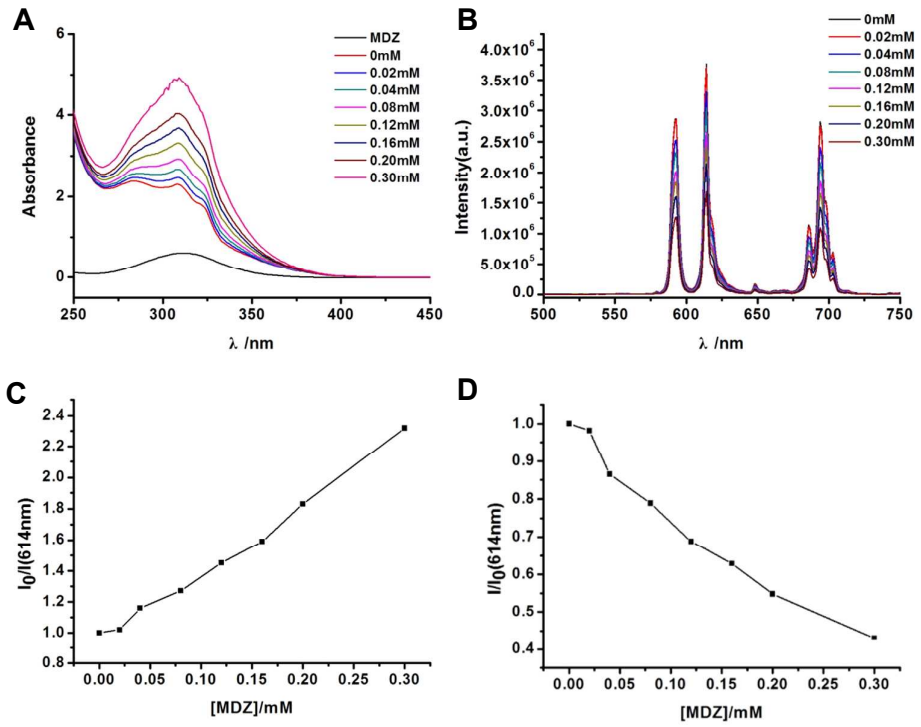

Figure S67. UV-vis absorption (A) and luminescence emission (B) spectra of titrating **3**^{R}-Eu with MDZ; luminescence quenching efficiencies I_0/I (C) and I/I_0 (D) of **3**^{R}-Eu with the addition of different amount of MDZ at 614 nm. ([**3**^{R}-Eu] = 0.02 mM in CH_3OH, λ_{ex} = 345 nm).

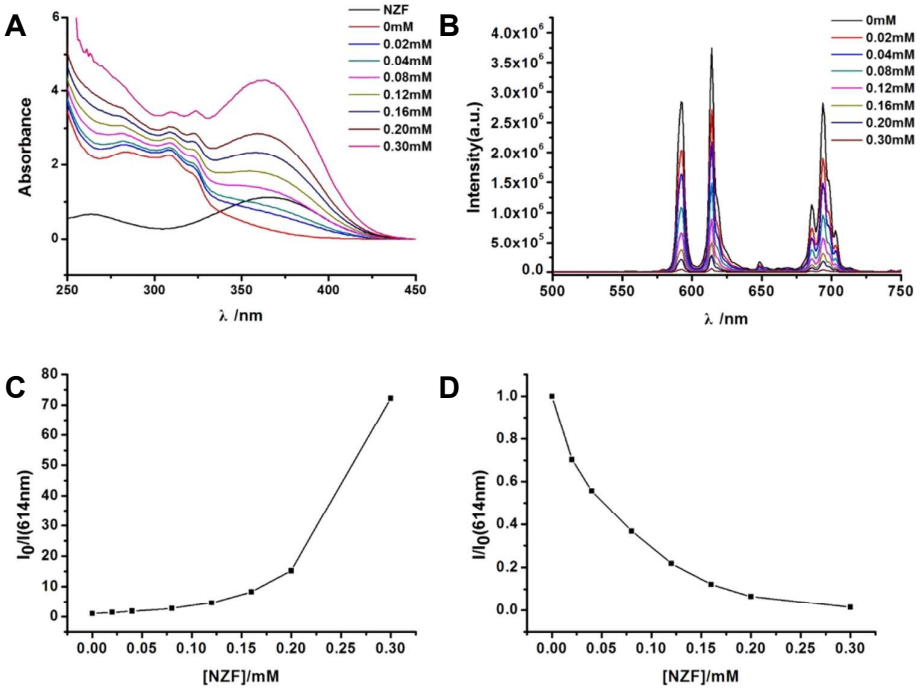

Figure S68. UV-vis absorption (A) and luminescence emission (B) spectra of titrating $\mathbf{3}^{R}$-Eu with NZF; luminescence quenching efficiencies I_0/I (C) and I/I_0 (D) of $\mathbf{3}^{R}$-Eu with the addition of different amount of NZF at 614 nm. ([$\mathbf{3}^{R}$-Eu] = 0.02 mM in CH_3OH, λ_{ex} = 345 nm).

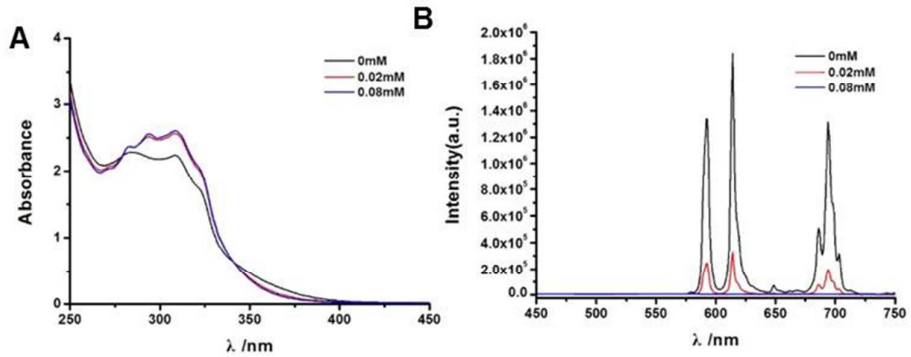

Figure S69. UV-vis absorption (A) and luminescence emission at 614 nm (B) spectra of cage $\mathbf{3}^{R}$-Eu after addition of AcOK. ([$\mathbf{3}^{R}$-Eu] = 0.02 mM in CH_3OH, λ_{ex} = 345 nm).

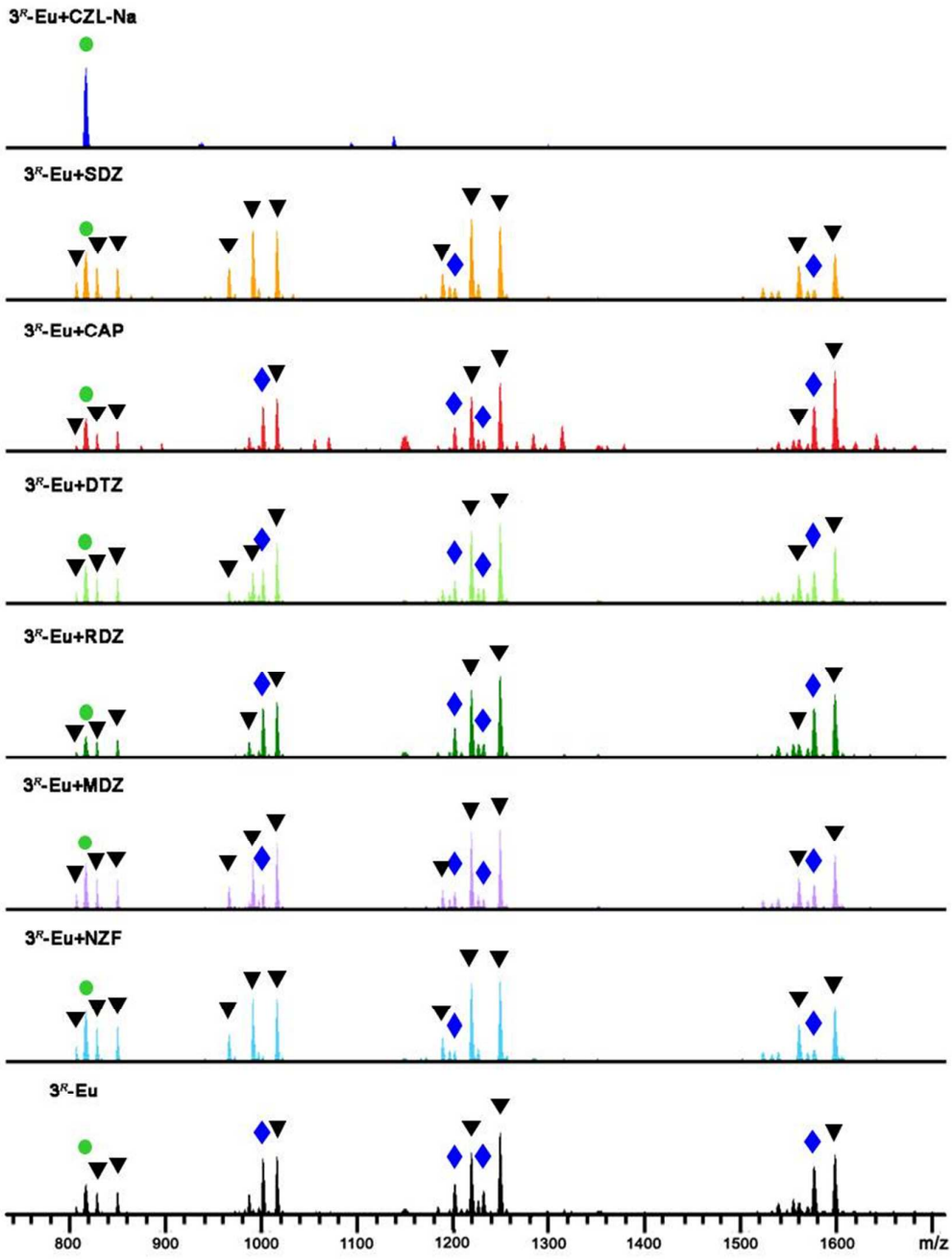

Figure S70. ESI-TOF-MS of $\mathbf{3}^{R}$-Eu after addition of 4.0 equiv of different antibiotics. Corresponding signals assignable for $\mathbf{2}^{R}$ (●), $\mathbf{3}^{R}$-Eu (▼) and $\mathbf{3}^{R}$-Eu•$(CH_3OH)_2$ (◆) are labeled.

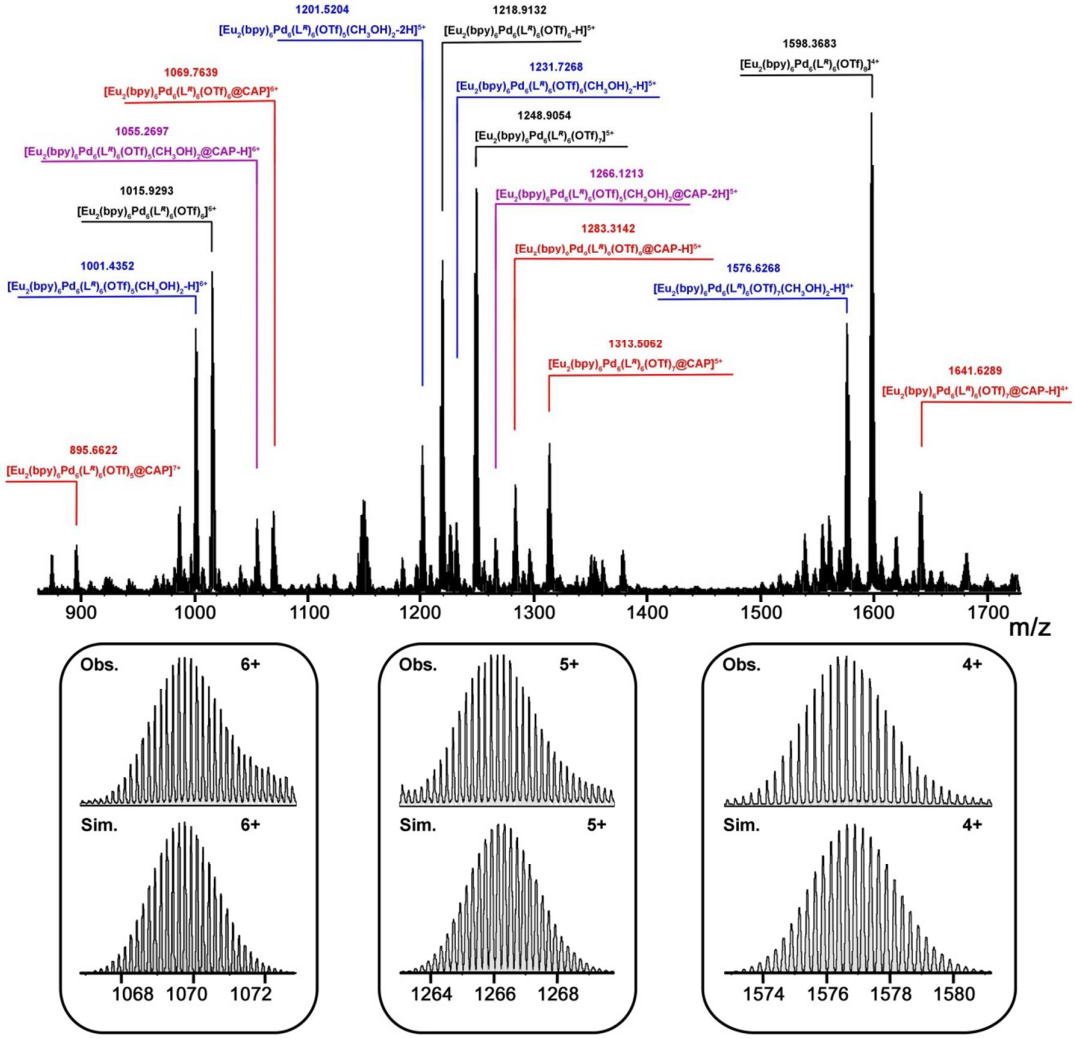

Figure S71. ESI-TOF-MS of $\mathbf{3}^{R}$-Eu after addition of 4.0 equiv of chloramphenicol (CAP) with insets showing the observed and simulated isotopic patterns corresponding to $[\mathbf{3}^{R}\text{-Eu(OTf)}_6\text{@CAP}]^{6+}$, $[\mathbf{3}^{R}\text{-Eu(OTf)}_5\bullet(CH_3OH)_2\text{@CAP–2H}]^{5+}$, $[\mathbf{3}^{R}\text{-Eu(OTf)}_7\bullet(CH_3OH)_2\text{–H}]^{4+}$.

5. DFT calculation:

Table S2。 Atomic coordinates of the optimized structure of ligand **1H**^{R}

N	-11.2009	0.0414	-1.5445
N	-11.7828	1.1239	-0.9746
C	-10.7768	1.7565	-0.3848
C	-9.5398	1.0823	-0.5624
C	-9.8671	-0.0288	-1.3305
C	-8.2433	1.5645	-0.0336
O	-8.1143	2.7115	0.3786
N	-7.227	0.6235	-0.0515
C	-5.8865	0.7612	0.3618
C	-5.4493	1.8678	1.07
C	-4.115	1.9326	1.5122
C	-3.2238	0.9172	1.2543
C	-3.6174	-0.2201	0.4991
C	-4.9749	-0.3056	0.034
C	-5.3655	-1.4389	-0.7288
C	-4.4763	-2.4551	-0.989
C	-3.1448	-2.3956	-0.5371
C	-2.7101	-1.291	0.175
N	-1.3694	-1.163	0.5968
C	-0.3501	-2.0958	0.5345
O	-0.4603	-3.2308	0.1055
N	2.0535	-1.9045	0.385
C	0.9653	-1.5752	1.0883
C	1.0183	-0.8485	2.287
C	2.2631	-0.4413	2.7614
C	3.398	-0.7544	2.0181
C	3.243	-1.488	0.8323
C	4.4399	-1.9009	-0.007
O	4.5045	-2.9894	-0.5569
N	5.4476	-0.9694	-0.0632
C	6.6005	-1.1785	-0.9625
C	7.6085	-2.1832	-0.3735
C	7.2186	0.1546	-1.3642
C	7.3102	0.4424	-2.713

C	7.8935	1.639	-3.1886
C	8.3811	2.5644	-2.2991
C	8.3079	2.3284	-0.9006
C	7.7245	1.1078	-0.4131
C	7.6782	0.918	0.9994
C	8.1722	1.866	1.8692
C	8.7432	3.0636	1.3813
C	8.8069	3.2838	0.0252
H	-11.7754	-0.595	-2.0776
H	-10.9436	2.676	0.1583
H	-9.2714	-0.8249	-1.7559
H	-7.5158	-0.3155	-0.2777
H	-6.1451	2.6638	1.2906
H	-3.797	2.7967	2.0889
H	-2.2236	0.9964	1.6687
H	-6.3622	-1.5079	-1.1533
H	-4.7922	-3.3145	-1.5735
H	-2.4496	-3.1928	-0.7565
H	-1.0783	-0.2309	0.8498
H	0.113	-0.6416	2.85
H	2.3476	0.1007	3.6992
H	4.3863	-0.4655	2.3613
H	5.2133	-0.0126	0.165
H	6.1988	-1.6429	-1.8706
H	8.082	-1.8126	0.5392
H	8.3961	-2.3814	-1.1084
H	7.0944	-3.1225	-0.1548
H	6.9225	-0.2744	-3.4326
H	7.9465	1.8204	-4.2584
H	8.8285	3.4912	-2.6502
H	7.2456	0.0089	1.4005
H	8.1257	1.6892	2.9405
H	9.13	3.8033	2.0768
H	9.2447	4.2002	-0.3639

6. References:

S1. Holz, R. C.; Chang, C. A.; Horrocks ,W. D. Jr. Spectroscopic Characterization of the Europium(III) Complexes of a Series of N,N'-Bis(carboxymethyl) Macrocyclic Ether Bis(1actones). *Inorg. Chem.* **1991,** *30*, 3270-3275.